U.S. DEPARTMENT OF
ENERGY

Office of
ENERGY EFFICIENCY &
RENEWABLE ENERGY

Batteries

Final Report

Vehicle Technologies Office

(This page intentionally left blank)

II Advanced Materials R&D

II.9 Beyond Li-ion R&D: Solid-State Batteries

II.9.D Lithium Dendrite-Free Li_7N_2I-LiOH Solid Electrolytes for High Energy Lithium Batteries (University of Maryland, College Park)

Chunsheng Wang, Ph.D, Principal Investigator
University of Maryland, College Park
Room 3236 Jeong H. Kim Engineering Building
College Park, MD 20742
E-mail: cswang@umd.edu

Duong Tien, DOE [Program/Technology Development] Manager
U.S. Department of Energy
E-mail: [tien.duong@ee.doe.gov]

Start Date: Oct. 1, 2019 End Date: May 17, 2024
Project Funding (FY20-24): $1,000,000 DOE share: $1,000,000 Non-DOE share: $250,000

Project Introduction

All-solid-state lithium batteries (ASSLBs) hold great potential to improve the safety and energy density of today's lithium-ion batteries by using non-flammable inorganic solid electrolytes. Solid electrolytes (SEs) are believed to prevent Li dendrite growth because of high mechanical strength and high Li^+ transference numbers. Significant advances in SE have been achieved, among which, $Li_7La_3Zr_2O_{12}$ (LLZO) and Li_2S–P_2S_5 (LPS) are the most promising SEs for bulk-type solid-state lithium batteries because of high ionic conductivities (>10^{-4} S/cm^2). However, in contrast to our expectations, the growth of lithium dendrites is not suppressed but is facilitated in LLZOs and LPSs regardless of dopants, porosity, and crystallinity of the electrolytes. Despite the unity Li transference number and over two-times of shear modulus than that of Li metal, the critical current densities for Li plating and stripping in these SEs are less than 1.0 mA cm^{-2}, which is one-fourth to one-tenth of that in liquid electrolytes at room temperature. The incompatibility between LLZO and LPS with Li metal seriously limits the energy density of all-solid-state batteries.

The mechanism for lithium dendrite formation and growth in SEs are still disputable. Lack of understanding of the Li dendrite formation mechanism seriously impeded the development of solid-state lithium batteries. The development of the criterion for Li dendrite suppression is essential for the success of solid electrolyte lithium batteries. In this project, a criterion for Li dendrite suppression will be developed through thermodynamics and kinetics analysis of lithium dendrite nucleation/growth, which will guide the solid-state electrolyte design. Li_7N_2I-LiOH, Li_5NI_2-LiOH and Li_3YCl_6 solid electrolyte with high ionic conductivity and low electronic conductivity were used to validate the criterion for lithium dendrite suppression. Different surface modifications were also explored to enhance the dendrite suppression capability of SSEs.

Objectives

The objective of this project is to research, develop, and test Li-metal-based batteries that implement solid Li-ion conductors (LICs) equipped with targeted solid electrolyte capable of achieving cell performance of 350 Wh/Kg energy density for 1000 cycle life with a cost of ≤ $100/kWh.

The main objective in the Budget Period 1, is to develop and optimize the targeted electrolytes. The tasks for the first budget period are (1) synthesis of targeted electrolytes with high ionic conductivity; (2)

electrochemical properties of targeted electrolytes; (3) Li dendrite suppression capability; and (4) High Coulombic Efficiency (CE) for Li plating/stripping.

In year one, the project will synthesize, modify, and optimize the targeted electrolytes to achieve a high ionic conductivity to > 5×10^{-4} S/cm Critical Current Density (CCD) of > 2.0 mA/cm^2 at a capacity of > 2.0 mAh/cm^2. The team will focus on enhancing the CE for lithium anode to > 99%. The CE of the solid electrolyte is a powerful indicator of electrolyte stability and lithium dendrite growth. The mechanism of Li dendrite growth in the targeted solid-state electrolytes and thermodynamic Li dendrite suppression criterion will also be developed.

Approach

Approach 1: The relationship among interface energy, Li plating/striping overpotential, interface resistance, solid electrolyte stability with Li, and CCD will be established. The dendrite suppression criterion will be developed based on the relationship. The dendrite suppression capability for the Li_7N_2I-LiOH pellet will be evaluated by testing the CCD.

Approach 2: The dendrite suppression criterion will be developed based on the Butter-Volmer model and total energy analysis. The dendrite suppression criterion will also be validated by using Li_3N-LiF, Li_7N_2I-LiOH and Li_7N_2I-LiOH/Li_3YCl_6 bi-layer electrolytes that are stable against Li metal together with high ionic conductivity and high interface energy against Li. New interface engineering methods will be explored based on the learned mechanisms on $Li_{6.5}La_3Zr_{1.5}Ta_{0.5}O_{12}$ (LLZTO) electrolyte.

Approach 3: Li metal surface will be engineered with the interface to suppress dendrite growth and maintain cycling stability. Thin-film solid electrolyte will be fabricated from solid electrolyte with modified particle size and polymer binder. A high energy density solid-state battery will be assembled by combining Li modification, thin-film solid electrolyte and thick and stable positive electrode.

Approach 4: Li metal surface will be engineered with the interface to suppress dendrite growth and maintain cycling stability. Thin-film solid electrolyte will be fabricated from solid electrolyte with modified particle size and polymer binder. A high energy density solid-state battery will be assembled by combining Li modification, thin-film solid electrolyte and thick and stable positive electrode.

Approach 5: We will design a lithiophobic current collector to achieve high-performance anode-free solid-state batteries. We will also apply a 3-dimensional lithiophobic and high ionic conductive layer to stabilize the halide electrolyte.

Accomplishments

Accomplishments 1.1 Synthesis, Characterization and Optimization of Li_7N_2I-LiOH, Li_5NI_2-LiOH and Li_3YCl_6 Electrolytes

Li_7N_2I-LiOH, Li_5NI_2-LiOH and Li_3YCl_6 were prepared through mild solid-state reaction and ball-milling. The Li_7N_2I-LiOH shows a high ionic conductivity of 0.14 mS/cm while that of Li_3YCl_6 is 0.48 mS/cm (**Figure 1.1.1a).** The activation energy of the Li_7N_2I-LiOH pellet is measured to be 0.34 eV. The ionic conductivity of Li_3YCl_6 is quite close to the goal of 0.5 mS/cm and the activation energy of the Li_7N_2I-LiOH meets the requirement of 0.34 eV. To improve the ionic conductivity of the Li_7N_2I-LiOH, we optimized the ratio of Li_3N, LiI, and LiOH. As shown in **Figure 1.1.1b**, the ionic conductivity of Li_5NI_2 can be significantly improved by doping LiOH. The Li_5NI_2-LiOH shows a high ionic conductivity of 0.8 mS/cm meeting the requirement of 0.5 mS/cm^2. **Figure 1.1.1d** shows the cyclic voltammetry (CV) curve of Li| Li_7N_2I-LiOH-Li_3YCl_6| SS cells at a scan rate of 1 mV/s. The CV indicates that Li_7N_2I-LiOH/Li_3YCl_6 bi-layer solid-state electrolyte enables a wide

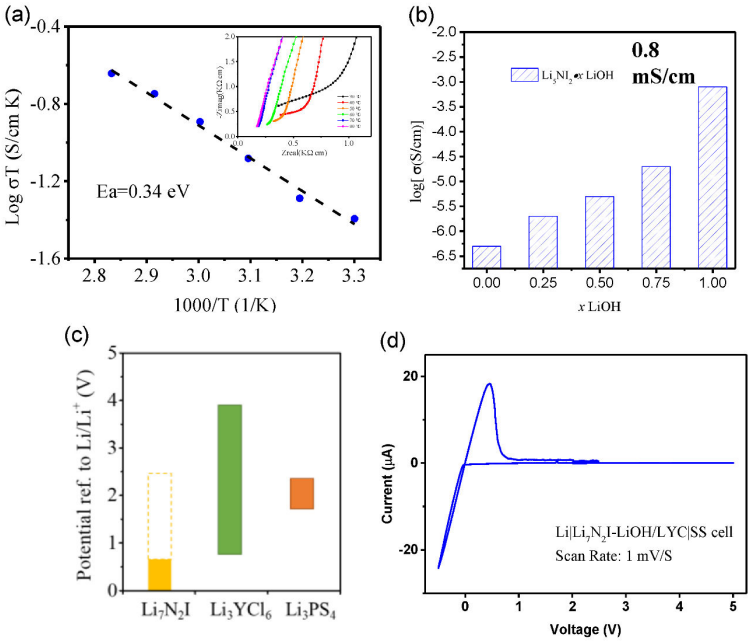

Figure 1.1.1 (a) ionic conductivities of Li_7N_2I-LiOH electrolyte at different temperatures from 25 to 80 °C. (b) Ionic conductivities of Li_5Ni_2-*x*LiOH with different amount of LiOH. (c) Calculated electrochemical stability window of Li_7N_2I, Li_3YCl_6 and Li_3PS_4. (d). Electrochemical stability window of the Li_7N_2I-LiOH |Li_3YCl_6 solid-state electrolytes using the cycle voltammetry test of a Li|SSE|SS (SS=stainless-steel) at the scan rate of 1 mV/s.

voltage window of 0-5 V. In **Figure 1.1.1c**, the electrochemical window Li_3YCl_6 is from 1.0V to 4.2V vs. Li^+/Li. Comparing to LPS, the electrochemical window of Li_7N_2I-LiOH/Li_3YCl_6 bi-layered electrolyte is significantly extended.

The SEM of Li_3YCl_6 and Li_7N_2I-LiOH pellets and the cross-section of the Li_7N_2I-LiOH/Li_3YCl_6 bi-layer solid-state electrolyte is shown in Figure 1.1.2. As we can see, the cold-pressed Li_3YCl_6 and Li_7N_2I-LiOH is rather dense. Moreover, Li_3YCl_6 and Li_7N_2I-LiOH in bi-layer electrolyte were close in contacted with each other.

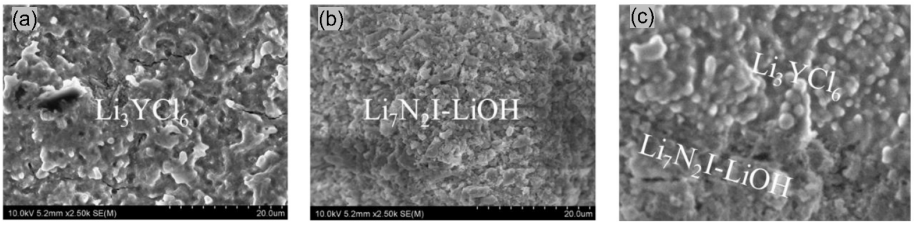

Figure 1.1.2 SEM images of (a) Li_3YCl_6, (b) Li_7N_2I-LiOH and the cross section of the cold-pressed pellets.

Accomplishments 1.2 Reduction of Li/Li_7N_2I-LiOH / Interface Resistance and the Dendrite Suppression Capability of the Li|Li_7N_2I-LiOH|Li Symmetry Cell

The Li_7N_2I-LiOH is thermodynamically stable with Li and has high interface energy, which causes large interfacial resistance. As shown in **Figure 1.2.1**, molten metallic Li is not wetted with Li_7N_2I-LiOH pellet surface, exhibiting a large contact angle. By surface coating, the contact angle of Li on Li_7N_2I-LiOH pellet surface becomes smaller. We use this method to assemble the Li|Li_7N_2I-LiOH|Li symmetry cell to measure the Li dendrite suppression capability of the solid-state electrolytes.

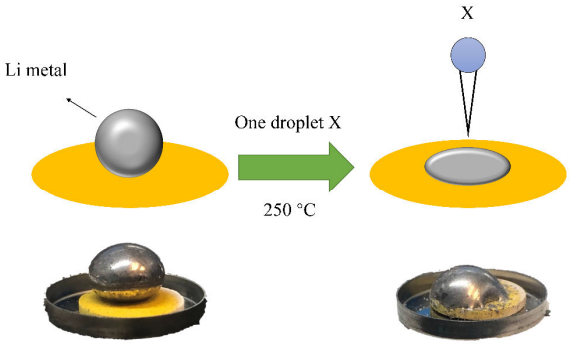

Figure 1.2.1 Scheme and digital picture of molten metal lithium on Li_7N_2I-LiOH pellet surface with and without surface treatment.

The Li dendrite suppression capability of Li_3N-LiI-LiOH electrolytes was evaluated using the CCDs. As shown in **Figure 1.2.2a**, the critical currents for both Li_7N_2I-LiOH and Li_5NI_2-LiOH electrolytes are higher than 2.0 mA/cm^2 at a capacity of 2.0 mAh/cm^2. **Figure 1.2.2b** demonstrates the cycle performance of Li|Li_7N_2I-LiOH|Li at a current density of 2.0 mA/cm^2 with a capacity of 2 mAh/cm^2. The overpotential slightly decreases at the first 5 cycles and becomes stable due to the penetration of Li metal into the porous of Li_7N_2I-LiOH electrolytes near the interface. Since the Li_7N_2I-LiOH electrolyte is thermodynamically stable and has high interface energy against Li, the Li penetration into porous Li_7N_2I-LiOH electrolyte is self-limited depending on the Li plating capacity. The Electrochemical Impedance Spectroscopy (EIS) plot of Li|Li_7N_2I-LiOH|Li before cycles, after the activation cycles, and after cycled at 2 mAh/cm^2 (**Figure 1.2.2c**) demonstrate that the Li_7N_2I-LiOH does not short and the decrease in overpotential is attributed to self-limited Li penetration. The decrease in the resistance is attributed to the enhancement of the contact between Li electrode and electrolyte due to the Li penetration into electrolytes. **Figure 1.2.2d** shows the cycle performance of Li|Li_5N_2I-LiOH|Li at a step-increased current density to 2.0 mA/cm^2 and capacity of 2 mAh/cm^2. The critical current of Li_5N_2I-LiOH is also higher than 2 mA/cm^2 at a capacity of 2.0 mAh/cm^2. The EIS of Li_5N_2I-LiOH electrolytes is shown in **Figure 1.2.2e**. The goal for a high critical current density of 2 mA/cm^2 in the Budget Period I have been reached. The mechanism of self-limited Li penetration into Li_7N_2I-LiOH is illustrated in **Figure 1.2.2f**.

The CE of Li plating and stripping of the Li|Li_7N_2I-LiOH|Cu cells is still under testing. A high CE of 99% was achieved for the Li_3N-LiF protected LPS electrolytes, which is attributed to the electrochemical stability of Li_3N-LiF protective layer against Li (**Figure 1.2.3**). We expected that CE of Li_3N-LiI-LiOH electrolyte should reach 99%. We will report the CE of Li_3N-LiI-LiOH electrolyte in the first-quarter report in Budget Period 2.

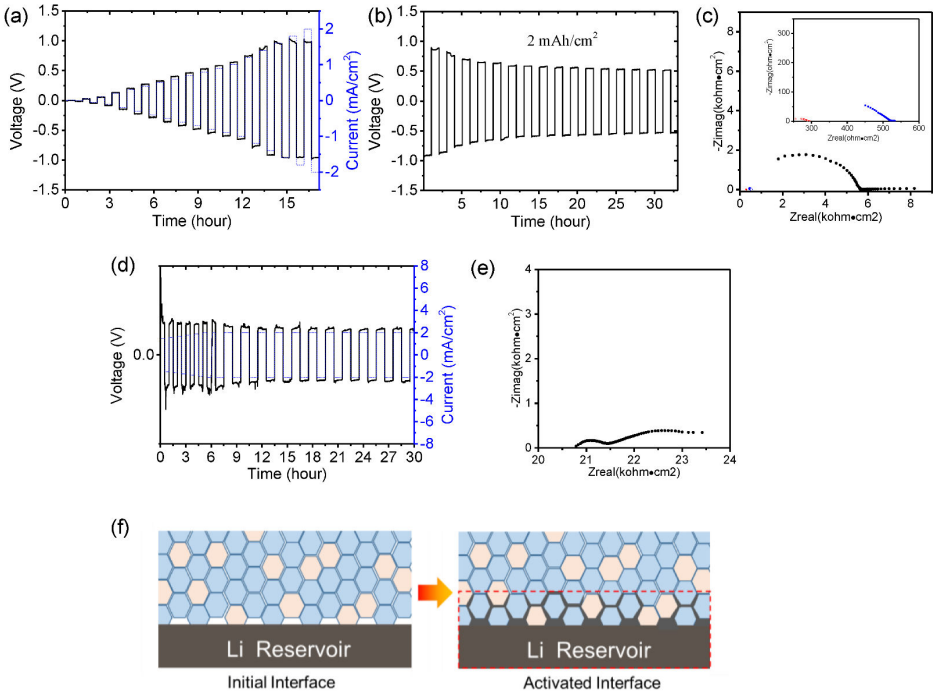

Figure 1.2.2 Electrochemical behavior of Li|Li_7N_2I-LiOH|Li and Li|Li_5NI_2-LiOH|Li cell. The Li plating/stripping behavior for the Li| Li_7N_2I-LiOH |Li cells (a) at a step-increase current for 0.5h; (b) at a current of 2 mA/cm^2 and the capacity of 2 mAh/cm^2; and (c) the EIS plot before cycle (black circle), after activation (blue circle), and after cycled at 2 mAh/cm^2 for 16 cycles. The Li plating/stripping behavior for the Li|Li_5N_2I-LiOH |Li cells (d) at a step-increase current for 0.5 h and 6 cycles and then at 2 mAh/cm^2 for 1.0 hour and (e) the EIS plot before cycles. (f) Scheme for self-limited Li penetration into Li_7N_2I-LiOH process.

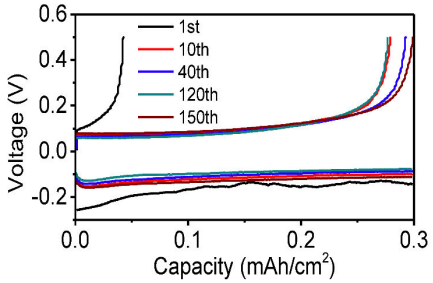

Figure 1.2.3 Li plating/stripping CEs in Li/Li_3N–LiF/LPS/Li_3N–LiF/SS cell at a current of 0.3 mA/cm^2 and voltage cut-off of 0.5 V.

Accomplishments 1.3 Development of Li dendrite suppression criterion for solid electrolytes

The Li dendrite nucleation and growth in SSEs depends on the energy landscape for Li deposition and stripping inside SSEs, which is represented by the Bulter-Volmer kinetics (**Figure 1.3.1a**). The parabolas on the left designates reaction coordinate of Li deposition ($Li^+ + e^- \rightarrow Li$) and the parabolas on the right designates that of Li stripping ($Li \rightarrow Li^+ + e^-$). At an open-circuit after the SSE contacting with Li metal, the activation energy and the reaction rate for Li plating in SSEs is much larger than Li stripping in SSEs (blue dashes in **Figure 1.3.1a**).

The difference in activation energy between Li plating and stripping increases with the increasing of interface energy and decreasing of electronic conductivity of the SSEs. Once the Li plating starts, the electrolyte potential up-shifts by η, Li plating driving energy inside SSE moved up by Fη, which reduces the energy barrier for Li plating inside electrolyte ($\Delta G'_{Li^+ + e \rightarrow Li}$) but increase energy barrier for the Li stripping ($\Delta G'_{Li + e \rightarrow Li^+}$). When the Li plating current reach to a critical current, in which the potential shift (overpotential) reaches to a critical value η* (critical overpotential), the activation energy of Li plating is the same as that of Li stripping in SSEs (red dashes in **Figure 1.3.1a**). Li dendrite will be formed in SSE when the overpotential is larger than critical overpotential η* where the current is larger than the critical current (I*=η*/ASR). The critical current is high when the activation energy difference between Li plating and stripping at open-circuit is large and area specific resistance (ASR) is low. Therefore, the critical current density of SSEs increases with increasing of interface energy against Li, increasing of the ionic conductivity (reducing ASR), and decreasing of electronic conductivity. Since the high interface energy of SSE can provide large interface tension to prevent Li dendrite nucleation and growth in SSE, especially at void, defect and grain boundary, highly dense SSE is not required. However, if SSEs are lithophilic with a much low interface energy against Li, SSEs should have a high dense with less grain-boundary defects since the large interface tension force Li to penetrate into the grain-boundary, especially at grain boundary and defects.

The impact of thermodynamic stability, interface energy and electronic conductivity of SSEs on the Li dendrite formation was summarized in **Figure 1.3.1b**. When the SSEs are stable with Li, electronic insulated and have low interface energy, Li dendrite grow from Li anode into grain boundaries (GBs) or hole of SSEs through mechanical Li infiltration due to the high interface tension and Li plating pressure. The mechanical Li dendrite growth mainly contributes to the intergranular growth, such as propagation in GBs, pores and cracks induced by Li growth (first row **Figure 1.3.1b**). However, if the local electronic conductivity of SSEs is high, the Li chemical potential in SSEs will drop to a negative potential similar to the Li plating anode, so Li can even directly nucleate and grow inside SSE. (second row in **Figure 1.3.1b**). Only if the SSEs are stable with Li have high interface energy against Li and insulated electronic conductivity, Li dendrite will not nucleate and grow inside SSEs, and not penetrate into SSEs because the high interface energy significantly increase the energy barrier of

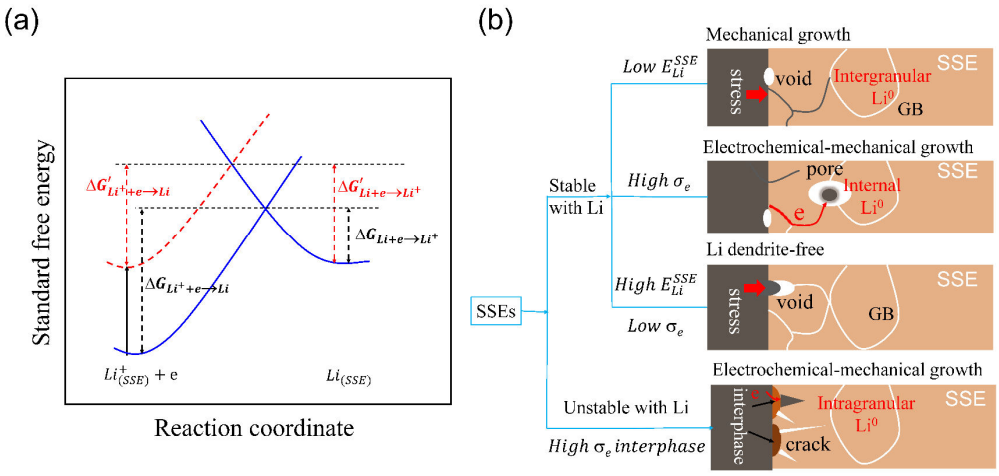

heterogeneous nucleation and the high interface tension between SSEs and Li also suppress Li propagation and penetration into SSEs (third row in **Figure 1.3.1b**). If the SSEs are unstable with Li, and the formed interphases have a high electronic conductivity, the electrochemical reaction between Li and SSEs accelerate the Li dendrite nucleation and growth in SSEs. The Li dendrite growth in SSEs changes from mechanical pattern to electrochemical-mechanical pattern. (fourth row in **Figure 1.3.1b**). The continuous side reaction between Li and electrolyte will unavoidably lead to high self-charge.

Figure 1.3.1 Li dendrite formation mechanism in SSEs. (a) Illustration of Butler-Volmer model for Li plating in SSE; (b) Li dendrite formation and growth mechanism in SSE with different properties.

Conclusions

We systematically investigated the composition of Li_xN_yI-zLiOH electrolytes (x=5, 7, 10, y=2, 3, z=0.25, 0.5, 0.75, 1) by mixing with different amount of Li_3N with LiI and LiOH. Li_5NI_2-LiOH and Li_7NI_2-LiOH were selected for further investigation. In addition, by replacing LiI with LiF, Li_3N-LiF electrolytes were also developed to investigate the Li dendrite formation mechanism. The principles of designing Li dendrite-free solid-state electrolytes have been published in *Advanced Materials* in October, 2020. The main achievements are summarized below.

- Development of Li_5NI_2-LiOH and Li_3YCl_6 solid-state electrolytes with high ionic conductivities of 0.8 and 0.5 mS/cm, respectively, reaching the milestone of $> 5 \times 10^{-4}$ S/cm.
- Both Li_5NI_2-LiOH and Li_7N_2I-LiOH electrolytes show a high lithium dendrite suppression capability with a critical current density of 2.0 mA/cm^2 at a capacity of 2.0 mAh/cm^2; reaching the milestone of CCD of $>$ 2.0 mA/cm^2 at a capacity of $>$ 2.0 mAh/cm^2.
- The Li_3N-LiF electrolyte has reached the 99% of Coulombic efficiency [*Advanced Material*s, 2020, 2002741]. The CEs of Li|Li_7N_2I-LiOH|Cu and Li|Li_5NI_2-LiOH|Cu cells are under testing.
- The electrochemical stability window is 0.0 to 2.5 V for Li_7N_2I-LiOH electrolyte and 0.0 to 5.0 V for Li_7NI_2-LiOH/Li_3YCl_6 bi-layer solid-state electrolyte.
- A Li dendrite suppression criterion has been proposed and validated in Li_3N-LiF/Li_3PS_4 based all-solid-state battery.

Key Publications

X. Ji, S. Hou, P-F. Wang, X. He, N. Piao, X. Fan, C. Wang, Solid-State Electrolyte Design for Lithium Dendrite Suppression. *Advanced Materials*, 2020, 2002741.

Accomplishments 2.1 Reducing the interface resistance and suppressing Li dendrite by interface modification.

Li|LLZTO|Li cells with different interface modifications were assembled. TheLLZTO pellets are from the same batch with the same thicknesses and diameters. As shown in **Figure 2.1.1a-c**, the Li|LLZTO|Li cells that were modified by carbon, Bi, and AgF showed critical overpotentials (COP) of 0.18, 0.16, and 0.15 V, respectively. The COP varies within a small region between 0.15-0.18 V. We proposed that the COP rather than CCD should be used as a criterion for the Li dendrite suppression capability of SSEs because (1) the COP is an intrinsic property of the solid electrolyte materials, while CCD is an engineering parameter associating with COP, electrolyte thickness, interface resistance, as well as ionic/electronic conductivity; (2) COP represents the maximum resistance for Li dendrite growth which associates with the electronic conductivity, density, mechanical strength, and interfacial energy.

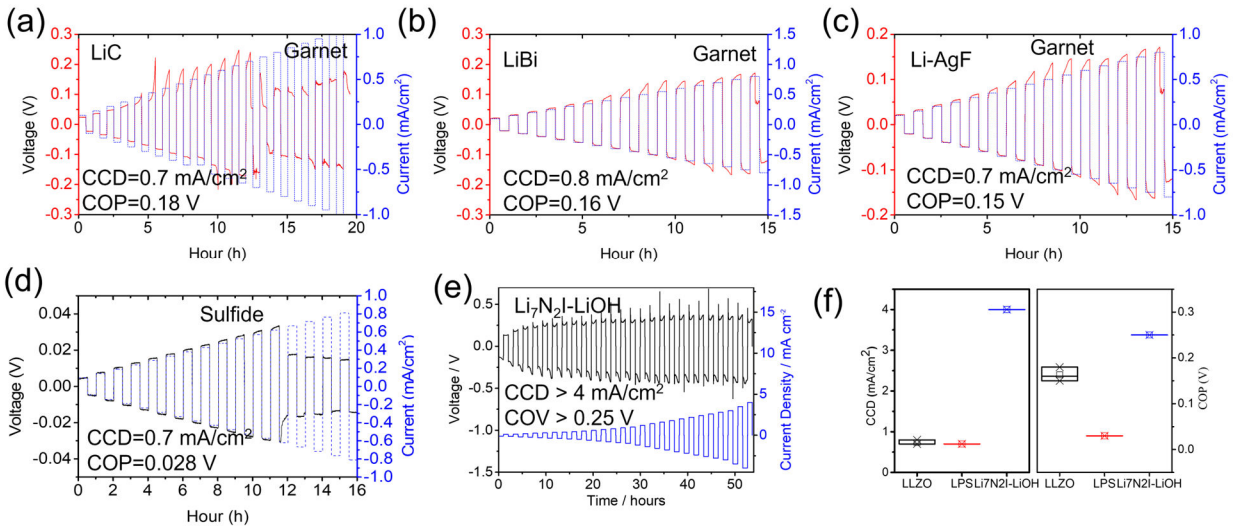

Figure 2.1.1 CCD and COP determined by the plating/stripping measurement with step-increased current. Li plating/stripping behaviors for different surface modifications with (a) graphite, (b) Bi and (c) AgF for Li|LLZTO|Li cell and (d) Li| Li_6PS_5Cl |Li and (e) Li|Li_7N_2I-LiOH|Li cells at a step-increased current. The determined CCD and COP are listed in the figures. (f) The box chart for the determined CCD and COP of different SSEs.

Moreover, CCD of a typical sulfide SSE Li_6PS_5Cl was also determined as 0.7 mA/cm^2 (**Figure 2.1.1d**), which is similar to the reported value. The corresponding COP of Li_6PS_5Cl SSEs is about 0.03 V. Although CCD of the two electrolytes (Li_6PS_5Cl and LLZTO) are close to each other (0.7-0.8 mA/cm^2), the COPs of sulfide electrolytes (0.03 V) are much lower than those of LLZTO electrolytes (0.15-0.18V) due to the less-stability of the sulfide electrolytes. The side reactions between Li and sulfide electrolytes result in cracks and new interphase formation with low interface energy against Li metal.

The COP of Li_7N_2I-LiOH pellets with similar size and thickness as those of oxides and sulfides was also investigated. As shown in **Figure 2.1.1e**, the COP of Li_7N_2I-LiOH is > 0.25 V, which is higher than the COPs of LLZTO. This may originate from the intrinsic stability of Li_7N_2I-LiOH against lithium metal. **Figure 2.1.1f** shows the box chart for the determined CCDs and COPs of Li_7N_2I-LiOH, LLZTO and LPS electrolytes. The COPs of Li_7N_2I-LiOH, LLZTO and LPS electrolytes reflect the stability of these electrolytes against Li, reconfirming that COP is a good indicator to reveal the intrinsic dendrite suppression capability of solid-state electrolytes.

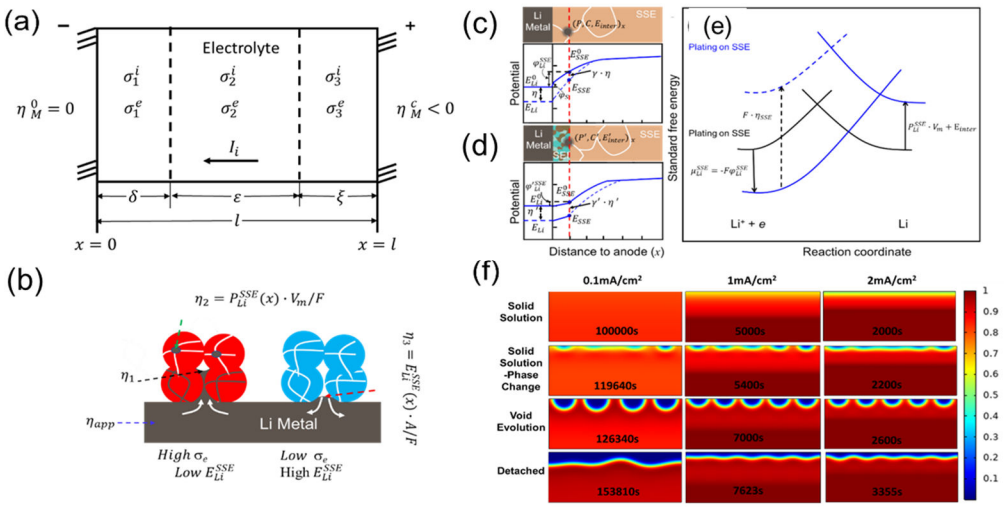

Figure 2.2.1 Thermodynamic and kinetics analysis for solid state battery. (a) Thermodynamic model of SSE for Li dendrite growth, whereσ_i, σ_e are ionic conductivity and electronic conductivity; $\nabla\eta_i$, $\nabla\eta_e$ are electrochemical potential gradients of ions and electrons, δ, ε and ξ (subscripts 1, 2 and 3) represent the areas for cathode interface, bulk SSE and anode interface. (b) Kinetics of Li dendrite growth in SSEs. Li dendrite growth in stable SSE which is not dense and has different electronic conductivity and interface energy, P_{Li}^{SSE} is the stress of Li nucleation site; E_{Li}^{SSE} is the interface energy of SSE against Li, V_m is the Li molar volume, and A is the interface area, F is the faraday constant. (c-d) 1D battery model near anode and their corresponding spatially dependent potential distribution in (c) stable and (d) unstable SSE. (e) Effects of a potential change on the standard free energy of activation for oxidation and reduction on Li metal (black lines) and SSE (blue lines). At the distance to anode of x, the stress, concentration of species i, and interface energy against Li metal are defined as $P(x)$, $C_i(x)$, and $E_{inter}(x)$ respectively. (f) Li metal diffusion kinetics at different applied current densities simulated by the phase-field model.

Accomplishments 2.2 Investigation of thermodynamics and kinetics of Li deposition process.

Using the model in **Figure 2.2.1a**, we developed the Li dendrite formation criterion in LLZTO and LPS. Consider a simple ionic solid where the conduction cations have a charge of +1, giving the equilibrium reaction:

$$\mathrm{M} \rightleftharpoons \mathrm{i} + \mathrm{e} \tag{1}$$

Based on basic electrochemical principles and reasonable assumptions, we can get:

$$\frac{\Delta\eta_M^{\delta}}{F} = \frac{\mathrm{A}\left[\frac{\Delta\eta_M^{c}}{F} + \frac{\sigma_2^i}{\sigma_3^i}V_T\right]}{1+\mathrm{A}} \tag{2}$$

where F is Faraday's constant, V_T and A are voltage and area, defined as $-\int_0^l \left(\frac{\nabla\eta_e}{F}\right)dx$ and $\frac{\delta}{l-\delta}\frac{\sigma_3^i}{\sigma_1^i}$ respectively. Ionic conductivity (σ_i) is defined under Ohmic current flow. According to equation (2), we can find that the critical overpotential $\Delta\eta_M^c$ for the cell will be affected by not only the Li|SSE interface but also the cathode|SSE interface. To suppress Li dendrite, a stable SSE is needed. If unstable, the interphase should have a high ionic conductivity and a low electronic conductivity.

Apart from the thermodynamic analysis of the SSEs, kinetics is also important for the stable operation of the all-solid-state battery. The Li dendrite growth in SSEs depends on driving force (applied Li plating potential, $\Delta\eta_M^{\delta}$) and resistance (critical Li plating overpotential in SSE, $\Delta\eta_M^c$). The $\Delta\eta_M^c$ is determined by the property of SSEs, including thermodynamic stability, ionic conductivity, electronic conductivity, porosity, interface energy and mechanical strength. Once the $\Delta\eta_M^{\delta}$exceeds the $\Delta\eta_M^c$, Li dendrites begin to grow. To suppress Li dendrite growth in SSEs, η_1 (also $\Delta\eta_M^{\delta}$) in **Figure 2.2.1b** needs to be reduced by increasing the ionic conductivity and reducing

electronic conductivity and surface resistance. Meanwhile, the $\Delta\eta_M^c = \eta_2 + \eta_3$ of SSEs should be increased by enhancing the local stress and interface energy of SSEs. For the electrolytes which are not dense, the Li infiltration into porous SSEs behaves like an incompressible work fluid, driven by the chemical potential/pressure gradient and interface energy of Li/SSEs. The dendrite can easily propagate in the SSEs with high electronic conductivity and low interface energy. However, for the SSEs which are electronic insulators with a high interface energy, the nucleation and growth should be suppressed.

To analyze the kinetics for the solid-state battery, the Bulter-Volmer equation based on the energy analysis and phase-field model was modified for the SSE and Li metal anode, respectively. **Figure 2.2.1c-e** shows the 1D model near the anode based on the Butler-Volmer equation and its corresponding spatially dependent potential distribution. According to the Butler-Volmer model, the Li plating current on Li metal (**Figure 2.2.1e** black lines) is related exponentially to the overpotential η. That is,

$$i_{Li} = FAk^0\left[C_{Li^+}(0,t)e^{-\alpha f\eta} - C_{Li}(0,t)e^{(1-\alpha)f\eta}\right] \quad (3)$$

where , A, k^0, α, and f are the frequency factor, standard rate constant, transfer coefficient and F/RT (R is gas constant and T is temperature). Accordingly, the potential in SSE will change from E_{SSE}^0 to E_{SSE}, resulting in an overpotential $\eta_{SSE} = E_{SSE} - E_{SSE}^0 = \gamma \cdot \eta$ in SSE (**Figure 2.2.1e** blue dashed lines), where γ is the overpotential transfer coefficient which is related to the electronic conductivity of the SSE. Moreover, the stress P and interface energy E_{inter} in the SSE will raise an opposite overpotential for Li deposit. The stress P is linear with the overpotential by $\eta_{stress} = P \cdot V_m/F$, where V_m is the molar volume of Li metal. Thus, the Li plating current in SSE i_{SSE} is

$$i_{SSE} = FAk^0\Big[C_{Li^+}(x,t)e^{-\alpha f(-\mu_{Li}^{SSE}(x)+\gamma\cdot\eta)} - C_{Li}(x,t)e^{[(1-\alpha)f(-\mu_{Li}^{SSE}(x)+\gamma\cdot\eta)+P_{Li}^{SSE}(x)\cdot V_m+E_{inter}]}\Big] \quad (4)$$

Consider the dendrite free situation, the i_{SSE} should be infinitely close to 0, thus,

$$C_{Li}(x,t) = C_{Li^+}(x,t)e^{[(1-\alpha)f(-\mu_{Li}^{SSE}(x)+\gamma\cdot\eta)+P_{Li}^{SSE}(x)\cdot V_m+E_{inter}]} \quad (5)$$

based on the equation, the summation of the overpotential should be as positive as possible to avoid the dendrite formation, requiring low electronic conductivity, high density and mechanical strength, and high interfacial energy.

Recent findings demonstrated that the kinetics of Li diffusion in Li metal anode plays a critical role in Li dendrite growth for all-solid-state batteries**. Figure 2.2.1f** shows the Li metal stripping process at an applied current density. At a stripping current of 0.1 mA/cm^2, a solid-solution Li diffusion process takes place with the decrease in density of Li metal at Li/SSE interface. After 119,640 seconds, some voids can be observed because of the phase transformation. At the time of 126,340 second, apparent voids formed on the Li/SSE interface and the Li anode completely detach from the SSE after 153,810 seconds. The morphology evolution of the Li metal results in a rapid increase of polarization during the stripping process. At a large current density of 1.0 and 2.0 mA/cm^2, the detachment between the Li metal and SSE are much earlier than that at 0.1 mA/cm^2. These results indicate that the kinetics for Li metal diffusion is very important for achieving a high COP and CCD.

Accomplishments 2.3 Tuning the lithiophobicity of the interface helps reduce interfacial resistance and suppress Li dendrite formation in LLZTO electrolyte

Different from all previous metal/metal oxide coatings on garnet or Li alloy anodes that form lithiophilic interlayer, Li-Sr/SrO-Li_2O is a lithiophilic/lithiophobic bifunctional layer **(Figure 2.3.1a-e**). This interlayer was demonstrated to simultaneouslyreduce the interfacial resistance and suppresses lithium dendrite. The optimized Li-Sr | garnet | Li-Sr symmetric cell can be cycled for 1,000 cycles under 0.5 mA/cm^2 (**Figure 2.3.1f**) with a critical current density of 1.3 mA/cm^2 at room temperature **(Figure 2.3.1g**). The good stability of the lithiophobic SrO doped Li_2O interphase prevents the garnet from reducing and suppresses Li dendrite, which distinguishes it

from all reported alloy electron-conducting interlayers. Therefore, the bifunctional lithiophilic/lithiophobic interlayer provides a new strategy for high-performance garnet solid-state lithium batteries (**Figure 2.3.1h**).

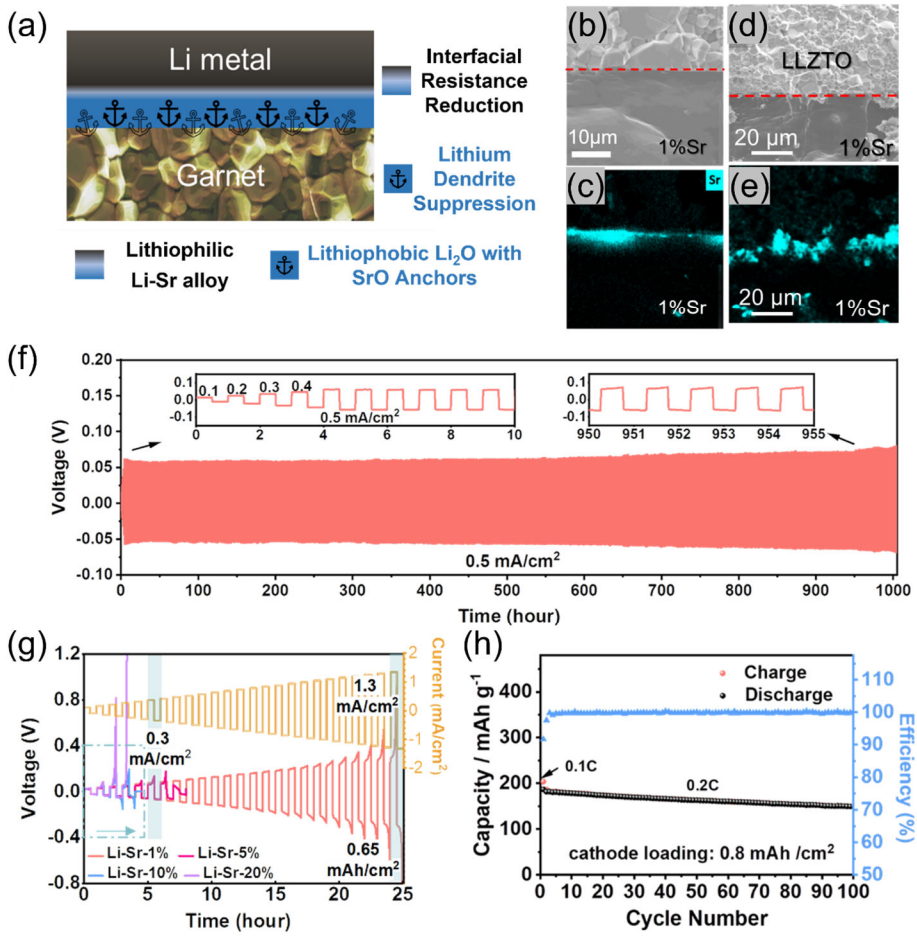

Figure 2.3.1 The interface design to reduce surface resistance and suppress Li dendrite in LLZTO electrolyte. (a)Schematic diagram of the bifunctional lithiophilic/lithiophobic interlayer. Cross-section morphology and Sr elemental mapping of the electrode interface with the LLZTO pellet before (b-c) and after (d-e) cycling showing a stable Sr segregation right on the interface. The red dash lines mark the interfaces. (f) Long-term cycling performance of Li-Sr | LLZTO | Li-Sr symmetric cell at 0.5 mA/cm^2. Inset is the magnification of the voltage profiles of 1-10 cycles and 950-1000 cycles. (g) The Li plating/stripping behavior for the cells at a step-increased current for 0.5 h. (h) The cycle performance for proof-of-concept Li-Sr | LLZTO | $LiNi_{0.8}Mn_{0.1}Co_{0.1}O_2$ (NMC811) cells at 0.2 C with cathode loading of 0.8 mAh / cm^2 (0.1 C for the first cycle for activation).

Accomplishments 2.4 Develop the thermodynamic stable Li_7N_2I electrolytes to suppress Li dendrite and realize ASSLBs

Li_7N_2I electrolyte was prepared by sintering a mixture of Li_3N and LiI at 550 °C. Multi-walled Carbon Nanotube (MWCNT) was purchased from Sigma Aldrich and fully dried before use. Fine Li_7N_2I powder was carefully mixed with 5 wt% MWCNT to use as the interface between Li_7N_2I electrolyte and Li anode. The Li-Li symmetry cell was first pre-cycled at a low current density of 0.1 mA/cm^2 to fully activate the interface. As can be seen in **Figure 2.4.1a**, the cell voltage of Li symmetric cell gradually decreases from 0.3 V and finally stabilizes at ~0.07 V. The stable cycling of the symmetric cell is due to the introduction of ionic/electronic conducting interface. We further studied the CCD of the Li_7N_2I with the designed interface in Li symmetric cells (**Figure 2.4.1b**). As can be seen, the cell voltage increases with the current density. Finally, a record-breaking high CCD of > 4.0 mA/cm^2 at a capacity of 4.0 mAh/cm^2 can be gotten before short-circuit occurs. On the other hand, the total

resistance of the Li symmetric cell based on electrochemical impedance spectroscopy (EIS) decreases from 2500 Ω cm^2 (**Figure 2.4.1c**) to 800 Ω cm^2 (**Figure 2.4.1d**) during the pre-cycling at 0.1 mA cm^{-2}. This process can effectively activate the interface and is essential to fully unleash the Li dendrite suppression capability of the interface. The Li dendrite suppression capability of the electrolytes with the designed electronic/ionic mixed-conducting interface was demonstrated by a high CCD. Although the total resistance of the Li symmetric cell is significantly reduced after cycling (**Figure 2.4.1e**), the EIS profile shows an obvious diffusion region at a low frequency of 0.1Hz, which indicates the cell has not been shorted by Li dendrite formation.

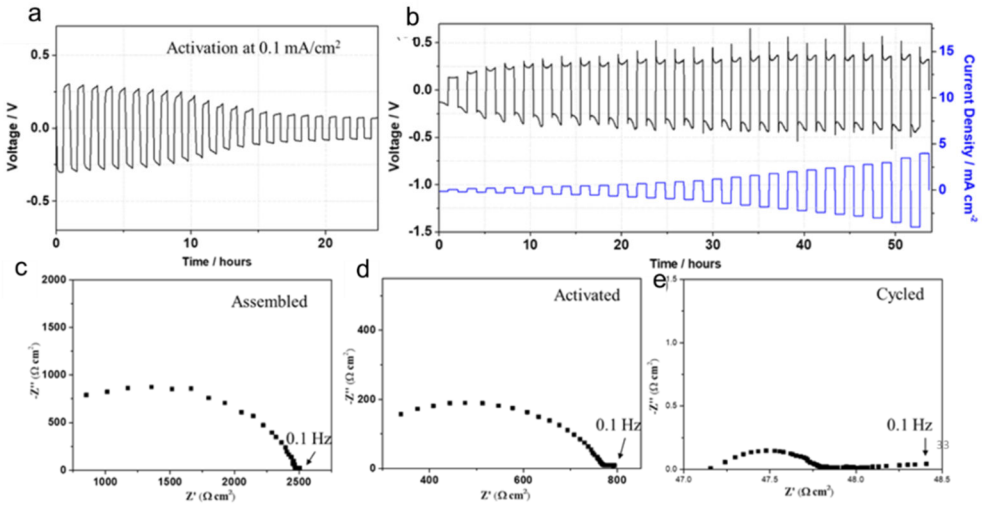

Figure 2.4.1 Li plating/stripping behavior of the Li_7N_2I-5% MWCNT protected Li_7N_2I electrolyte in Li symmetric cell configuration at room temperature. (a) Galvanostatic cycling of the Li symmetric cell at a current density of 0.1 mA cm^{-2}. (b) Voltage profiles of the cell under step-increased current densities from 0.2 to 4.0 mA cm^{-2} for Li plating/stripping with a fixed time of 1h. (c-e) Nyquist plots of the symmetric cell under different conditions: (c) before cycle (d) after activation, and (e) after cycled at 4 mAh cm^{-2} for 600 cycles.

Conclusions

- We determined the critical overpotential of Li_7N_2I-LiOH, LPS, and LLZO electrolytes.
- We developed both thermodynamic and kinetic models for the Li dendrite suppression criterion in solid-state electrolytes.
- A bifunctional lithiophilic/lithiophobic interlayer rich of Li-Sr/SrO-doped-Li_2O was proposed to suppress Li dendrite formation for garnet electrolytes.
- High CCD was demonstrated by Li_7N_2I-LiOH electrolyte with ionic-electronic mix conducting interface.

Key Publications

1. T. Deng, X. Ji, L. Zou, O. Chiekezi, X. Fan, L. Cao, T. R. Adebisi, H. Chang, H. Wang, B. Li, X. Li, C. Wang, D. Reed, J.-G. Zhang, V. Sprenkle, C. Wang, X. Lu, Interfacial engineering enabled practical low-temperature sodium metal battery, *Nat. Nanotechnol.,* **2022, 17**, 269–277.

2. X. He, X. Ji, B. Zhang, N. Rodrigo, S. Hou, K, Gaskell, T. Deng, H. Wan, S. Liu, J. Xu, B. Nan, B, Lucht, C. Wang, Tuning interface lithiophobicity for lithium metal solid-state batteries, *ACS Energy Lett*., **2021**, accept.

3. H. Wan, B. Zhang, S. Liu, J. Zhang, X. Yao, C. Wang, Understanding LiI-LiBr Catalyst Activity for Solid State Li_2S/S Reactions in an All-Solid-State Lithium Battery, *Nano Lett*. **2021**, 21, 8488-8494.

4. H. Wan, S. Liu, T. Deng, J. Xu, J. Zhang, X. He, X. Ji, X. Yao, C. Wang, Bifunctional Interphase-Enabled $Li_{10}GeP_2S_{12}$ Electrolytes for Lithium-Sulfur Battery, *ACS Energy Lett*., **2021**, 6, 862-868.

5. X. Ji, S. Hou, P-F. Wang, X. He, N. Piao, X. Fan, C. Wang, Solid-State Electrolyte Design for Lithium Dendrite Suppression, *Adv. Mater*. **2020**, 2002741.

Accomplishments 3.1 Suppressing Li dendrite by introducing composite polymer layer (CPI)

Generally, the interface film or SEI will be formed between the SSEs and Li anode via electrochemical or chemical reactions. Compared with the SSE-derived SEI, the introduced SEI can be denser and more ion-conductive via the interface engineering. **Figure 3.1.1a** shows the prepared gel-electrolyte, which is solid in room temperature and melt after heating to 40 °C or higher. The composite polymer has been reported to enable a stable cycling of Li||Li cells over 1000 h, indicating a uniform Li dissolution/deposition based on dynamic stability mechanism because of the formation of robust SEI and the confinement of solvent molecule of the polymer. The CPI was then applied to the full cell to evaluate its performance. **Figure 3.1.1b** shows the schematic of the ASSLMB, which utilizes the LPSC and LYC film as the thin electrolyte. The ratio of NMC622, LYC and carbon black is 70: 26:4, while the eLi with a design of CPI is used as the anode. The eLi/LPSC-LYC/NMC622 full cells were tested between 2.8 V and 4.2 V at RT under a stacking pressure of 8-10 MPa. The ASSLMB based on the designed eLi anode presents excellent rate capability when charged/discharged with different C-rates ranging from 0.1 to 1.0 C (**Figure 3.1.1c-d**). The cell can deliver high capacities of 165, 147, 118, and 76 mAh g^{-1} at C-rates of 0.1, 0.2, 0.5 and 1.0 C, respectively, while showing a high average CE of >99%. Long term cycling performance was also evaluated with the full cell at 0.15 C as shown in **Figure 3.1.1e**. The proposed SSB has an 81 % capacity retention after 100 cycles without sharp capacity drop, which is benefited from the robust SEI layer formed the CPI to effective block Li filament penetration. The CE of full cell with eLi is around 99.5% on average, which is much higher than the cell with fresh Li anode.

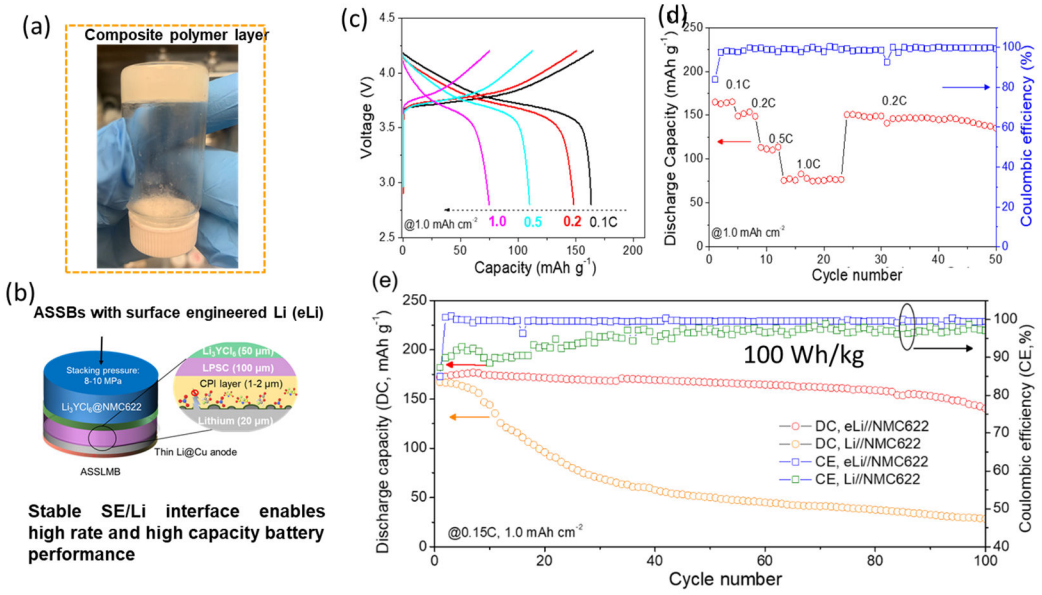

Figure 3.1.1 (a) Digital image of the gel-like electrolyte. (b) Schematic of the solid-state full cell with the designed eLi anode. (c) Charge-discharge curves of the cell at rates of 0.1, 0.2, 0.5, and 1.0 C. (d) Cycling performance of eLi/LPSC/NMC622 solid cell at 0.2 C with an areal capacity of 1.0 mAh cm^{-2}, 1C = 160 mA g^{-1}. (e) Comparison of the cycling performance of NMC622 solid full cell with fresh Li and eLi anodes at 0.15C, the cathode has an areal capacity of 1.0 mAh cm^{-2}.

Accomplishments 3.2 Fabricating thin-film LPSC-polymer composite electrolytes for high energy density

In order to achieve a high energy density of the ASSLB, a thin and robust solid electrolyte is required as illustrated in **Figure 3.2.1a**. To fabricate free standing thin-film electrolyte, 0.5wt% of acrylonitrile butadiene rubber (NBR) binder was mixed with wet-milled LPSC powder and pressed at 180 MPa. With the free-standing thin film electrolyte, we are able to design ASSBs with high energy density. Two designs are proposed (**Figure 3.2.1b**). In design I, 31.25 mg of composite cathode, 15 mg electrolyte and thin Li was used, which can reach an energy density of 350 Wh/kg. **Figure 3.2.1c** shows the SEM image and EDS mapping of full cell using design I. As we can see, a ~ 50 μm thin electrolyte sandwiched between Li and composite cathode. However, the cell

was short circuit during 1st charge, probably due to heterogenous stress distribution during Li plating, which will lead to electrolyte crack and cell short-circuit. To avoid the mechanical breakdown, we increase the electrolyte mass to 30mg and reduce the cathode load to 12.5 mg, which was marked as design II. The designed thin-film battery with lower cathode loading can be charged/discharged for 9 cycles (**Figure 3.2.1d**) and the cell can deliver a theoretical energy density of 153.5 Wh/kg.

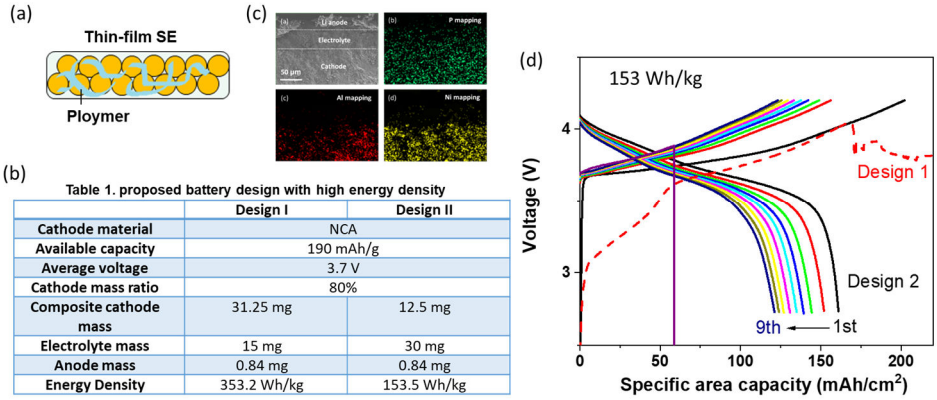

(b)

Table 1. proposed battery design with high energy density

	Design I	Design II
Cathode material	NCA	
Available capacity	190 mAh/g	
Average voltage	3.7 V	
Cathode mass ratio	80%	
Composite cathode mass	31.25 mg	12.5 mg
Electrolyte mass	15 mg	30 mg
Anode mass	0.84 mg	0.84 mg
Energy Density	353.2 Wh/kg	153.5 Wh/kg

Figure 3.2.1 (a) Schematic of the proposed thin-film solid electrolyte. (b) EDS mapping of the full cell with the thin-film electrolyte of the design 1. (c) charge-discharge curves of full cells with design 1 (dash line) and design 2 (solid line) in Table 1. (d) table of the proposed battery with different structure.

Accomplishments 3.3 High mass loading cathode enabled by Li anode modificaition

Li anode modification is also an effective way to increase the energy density of full cells. As shown in **Figure 3.3.1a**, we developed a modified Li anode that shows high critical current density of 8.0 mA/cm^2 at a fixed capacity of 4.0 mAh/cm^2 at temperature of 80 °C. Due to high Li dendrite suppression capability of modified Li anode, a high cathode loading was able to match with modified Li to assembled the NMC811||Li full cell, which can provide a high capacity of 7.9 mAh/cm^2 at current density of 1 mA/cm^2 and temperature of 80 °C (**Figure 3.3.1b**). The schematic of structure was shown in **Figure 3.3.1c.** The cells were assmbled by 70 mg of composition cathode with NMC811 weight raiot of 60% and the high weight of the electrolyte layer (25mg). The cell-level energy density was 223.8 Wh/kg for the assembled NMC811 full cell using the modified Li anode (**Figure 3.3.1d**).

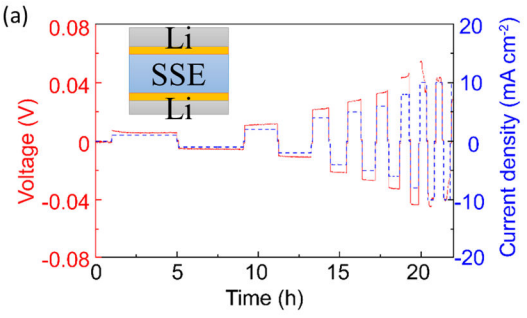

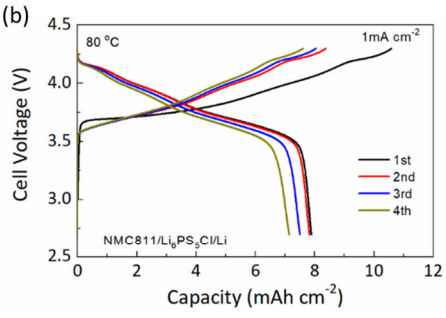

(c)

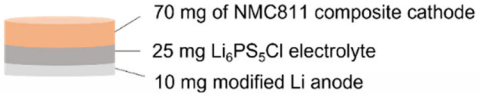

(d)

Cycle Index	Charge energy	Discharge energy	Charge energy density	Discharge energy density
1st	32.4 mWh	23.5 mWh	308.6 Wh kg^{-1}	223.8 Wh kg^{-1}
4th	23.4 mWh	21.1 mWh	222.9 Wh kg^{-1}	201 Wh kg^{-1}

Figure 3.3.1 (a) Critical current density of Li/LPSC/Li symmetric cell at fixed capacity of 4 mAh/cm^2 under 80 °C. (b) Cycling performance of the Li||NMC811 cell. (c) Schematic of the proposed thick cathode solid-state battery. (d) Table of calculated energy density of the corresponding battery.

Accomplishments 3.4 Optimizing the structure of solid-state batteries for higher energy density and lower cost

In the previous sections, we have evaluated three cell structures for high energy density, long cycling stability and low cost. The energy density comparisions were shown in **Figure 3.4.1a** and the detailed structural parameters were listed in **Figure 3.4.1b.** Structure 1 could provide stable cycling performance with 81% of retention after 100 cycles. However, the use of double-layer electrolyte limits the energy density. Moreover, yttrium(III) chloride is a expensive ingredient to prepare LYC elelctrolyte, which also increase the cost. Structure 2 replace the double layer electrolyte with solvent-modified LPSC. As a result, the energy density increases from 100 Wh/kg to 153 Wh/kg (**Figure 3.4.1a**). The energy density change is not significant because the cathode loading is still small. To solve the remaining issue, modified Li anode was use to macth with 78.5 mg of composite NMC811 cathode. The structure 3 NMC811||Li full cell can provide a high capacity of 7.9 mAh/cm^2 at current density of 1 mA/cm^2 and temperature of 80 °C. The cell-level energy density was >250 Wh/kg for the assembled NMC811 full cell using the modified Li anode. The low energy density is caused by the low weight ratio (60%) of NMC811 in the composite cathode and the high weight of the electrolyte layer (25mg). If the weight of the LPSC electrolyte layer can decrease to 10 mg, and the weight ratio of NMC811 in the composite cathode can be improved to 85%, the whole weight of the cell will be reduced from 105 mg to 69.4 mg, which will increase the cell-level energy density to 338.6 Wh/kg. We will further optimize the NMC811 composite cathode and the thin-film electrolyte layer in our further work. Due to structure 3 is the most promising design to reach higher energy density, the cost evaluation was further performed. Pie chart in **Figure 3.4.1c** shows that solid electrolyte will take up 91.91% of cell cost if the commercial LPSC electrolyte was used. This is because the manufactory of solid electrolyte is still in infancy. Therefore, the unit price of solid electrolyte is much higher than that of anode and cathode. By adopting the price of raw material for solid electrolyte (**Figure 3.4.1d**), the cost percentage of LPSC electrolyte in design 3 was dramatically reduced to 57%. The estimated cost for structure 3 is $208.8 /kWh. 90% further price reduction can be expected with the large-scale manufactory of solid electrolyte. Due to absence of transition metal, the inspeculation is reasonable. Therefore, structure 3 using modified Li anode and thin LPSC electrolyte is a promising choice to realize high energy density solid-state batteries.

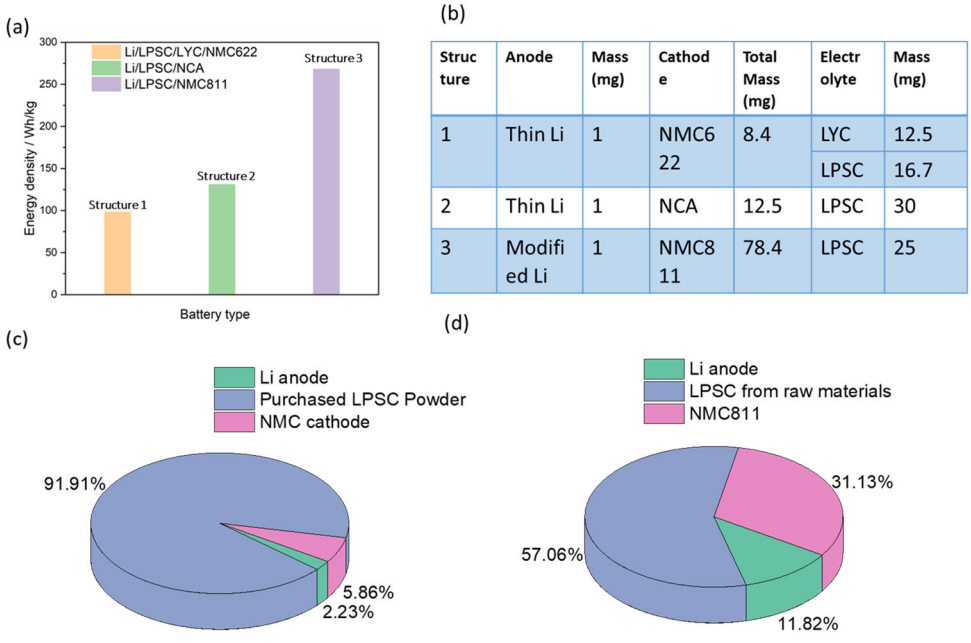

Structure	Anode	Mass (mg)	Cathode	Total Mass (mg)	Electrolyte	Mass (mg)
1	Thin Li	1	NMC622	8.4	LYC	12.5
					LPSC	16.7
2	Thin Li	1	NCA	12.5	LPSC	30
3	Modified Li	1	NMC811	78.4	LPSC	25

Figure 3.4.1 (a) Calculated energy density of three structural designs. (b) Structural parameters of three evaluated cell structure (c) Cycling performance of the Li||NMC811 cell. (c,d) Cost evaluation for structure design 3. The prices of LPSC was adopted from commercial in c and from raw materials in d.

Conclusions

- We engineered Li anode with a rational designed gel-electrolyte to achive stable cycling of NMC622 solid full cell with energy density of 100 Wh/kg for 100 cycles with a retention of 81%.
- We fabricated NCA || Li full cell using thin film composite electrolyte of polymer and microstructural optimized LPSC to reach energy density of 153 Wh/kg.
- A high critical current density of 8 mA/cm^2 at a fixed capacity of 4.0 mAh/cm^2 was achieved using modified Li anode.
- We developed a NMC811||Li full cell with high specific energy design of 223 Wh/kg, low cost by matching thick electrode with modified Li anode.

Key Publications

1. X. He, X. Ji, B. Zhang, N. Rodrigo, S. Hou, K, Gaskell, T. Deng, H. Wan, S. Liu, J. Xu, B. Nan, B, Lucht, C. Wang, Tuning interface lithiophobicity for lithium metal solid-state batteries, *ACS Energy Lett*., **2022,** 7 131-139.

2. T. Deng, X. Ji, L. Zou, O. Chiekezi, X. Fan, L. Cao, T. R. Adebisi, H. Chang, H. Wang, B. Li, X. Li, C. Wang, D. Reed, J.-G. Zhang, V. Sprenkle, C. Wang, X. Lu*,* Interfacial engineering enabled practical low-temperature sodium metal battery*, Nat. Nanotechnol.,* **2022,** 17, 269-277.

3. Hongli Wan, Zeyi Wang, Sufu Liu, Tao Deng, Xinzi He, Weiran Zhang, Chunsheng Wang, Critical Interphase Overpotential as a Lithium Dendrite Suppression Criterion for All-Solid-State Lithium Battery Design. *Nature Energy*, **2023**, 8, 473-481.

4. Xiao Ji, Xinzi He, Chi Chen, Singyuk Hou, Jijian Xu, Bao Zhang, Yunjun Ruan, Jiaxun Zhang, Tao Deng, Ji Chen, Chunsheng Wang, Void Suppressive Lithium Anodes for All-Solid-State Batteries, Nature Materials, Under review.

5. H. Wan, B. Zhang, S. Liu, J. Zhang, X. Yao, C. Wang, Understanding LiI-LiBr Catalyst Activity for Solid State Li_2S/S Reactions in an All-Solid-State Lithium Battery, *Nano Lett*. **2021**, 21, 8488-8494.

6. H. Wan, S. Liu, T. Deng, J. Xu, J. Zhang, X. He, X. Ji, X. Yao, C. Wang, Bifunctional Interphase-Enabled $Li_{10}GeP_2S_{12}$ Electrolytes for Lithium-Sulfur Battery, *ACS Energy Lett*., **2021**, 6, 862-868.

7. X. Ji, S. Hou, P-F. Wang, X. He, N. Piao, X. Fan, C. Wang, Solid-State Electrolyte Design for Lithium Dendrite Suppression, *Adv. Mater*. **2020**, 2002741.

Accomplishment 4.1: Modeling the Li plating and striping behaviors in the interlayer with different lithiophobicity.

Lithiophobicity of the interlayer significantly changes the Li growth from Li anode and nucleation inside the interlayer. Interlayers with different lithiophobicity exert different capillary forces on protruded Li. To analyze the influence of lithophobicity on Li penetration, Li penetration into a cylindrical shape pore was modeled as **Figure 4.1.1.a-b** by phase field methods. Li easily fills the conical shape surface flaw if the interlayer is lithiophilic (**Figure 4.1.1.a**). In contrast, Li penetration into conical shape surface flaw is self-limited in lithiophobic interlayer (**Figure 4.1.1.b**). Lithiophobicity of the interlayer significantly also changes the Li nucleation inside the interlayer. Li nucleation rate in mixed conductive interlayer was determined based on classical nucleation theory. As can be seen from **Figure 4.1.1.c**, the nucleation rate is a function of overpotential. When the overpotential reaches a certain value, the nucleation rate suddenly rises. The overpotential where observable nucleation occurs is defined as the critical nucleation overpotential η_c. The lithiophobicity of the interlayers, which was indicated by the contact angle of Li on the substrate, influences the critical nucleation overpotential η_c. Increasing the lithiophobicity of the interlayer can suppress the Li nucleation. For interlayer with a contact angle of 60°, the Li nucleation occurs with overpotential > 0.5 V and Li nucleation only occurs in the region close to Li anode (inserted). Further increasing the contact angle to 120° increase the overpotential to ~ 0.9 V in a small channel. Therefore, the lithiophobicity of the interlayer is a vital parameter to control Li nucleation and achieve stable plating.

Li striping from the porous interlayer was also studied with phase field methods. **Figure 4.1.1.d** shows the Li striping from the porous interlayer. To simulate Li stripping, the electrolyte channels are first filled with Li. The stripping was initiated by setting the potential as 0.1 mV. As we can see, the stripping behavior is quite non-uniform. From 0 – 1.5 s, Li stripping is concentrated on the bottom left region and right region. The fast stripping at the bottom left region is due to a smaller channel, which can provide more intimate contact. The right region also stripped fast, which can be explained by the short diffusion length to the counter electrode. When Li stripping continued from 1.5 – 3 s, some part of Li is isolated from current collect due to non-uniform stripping. Due to loss of contact with current collector, those Li cannot be stripped anymore. This is so called "dead lithium", which will cause low efficiency in ASSB. Therefore, dead lithium is a critical issue for porous interlayer. Designing a mixed ionic and electronic conductive interlayer can solve this problem.

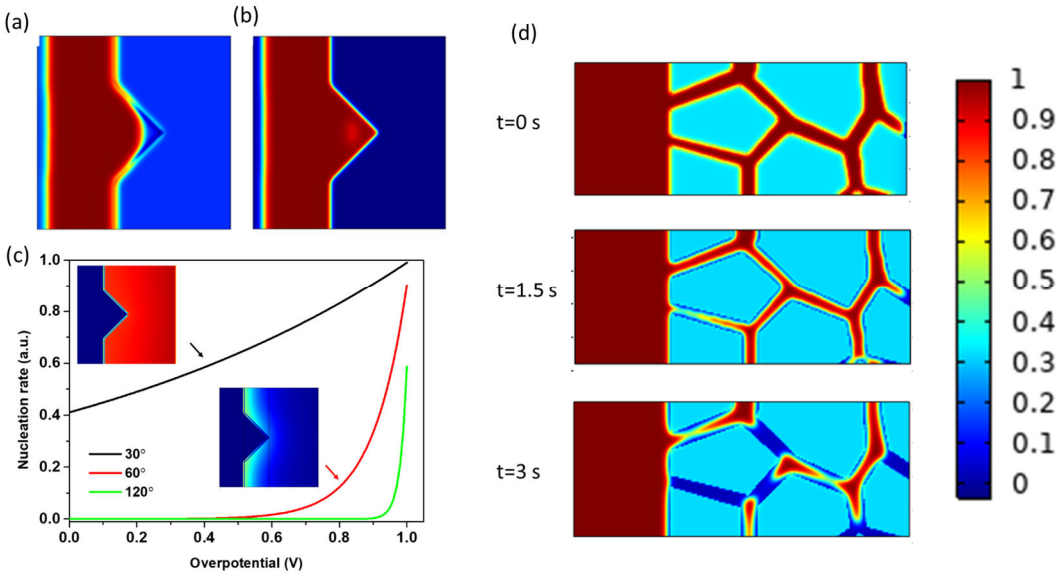

Figure 4.1.1 Phase field simulations of Li penetration into interlayer with different lithiophobicity. Li growth on a simplified conical shape surface flaw of the (a) lithiophobic interlayer and (b) lithiophilic interlayer. (c) Nucleation rate as a function

of overpotential at electrolyte with different contact angle against Li. The inserted figure shows the simulated Li nucleation rate distribution in the corresponding interlayer. (d) Li striping from porous interlayer at 0, 1.5 and 3 s.

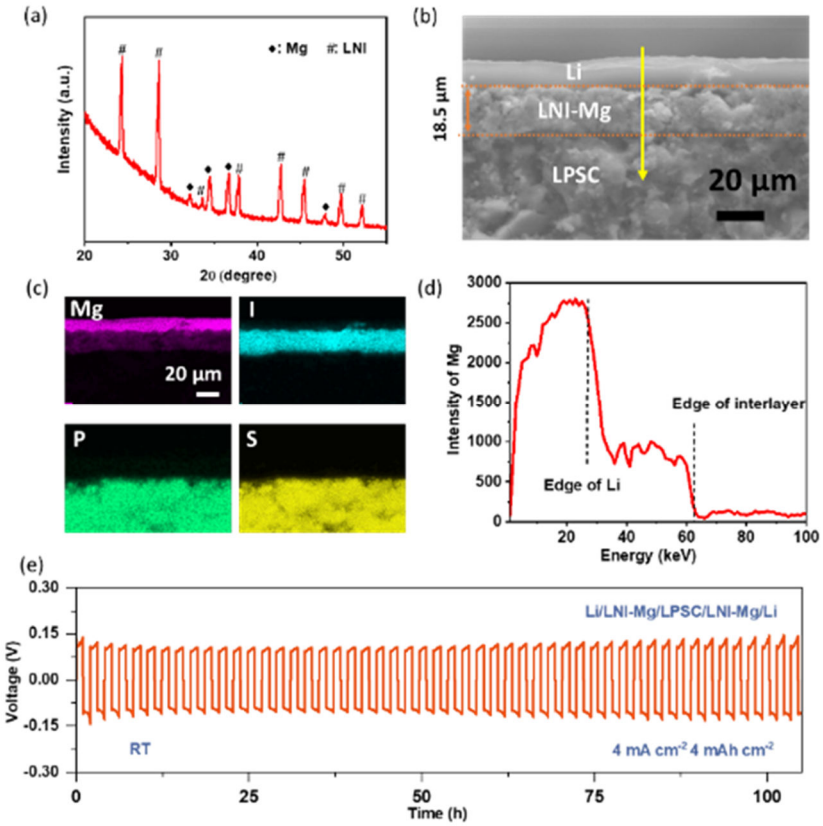

Figure 4.2.1 (a) XRD of LNI-25%Mg powder. (b) SEM, (c) EDS mapping and (d) Mg element line scan of activated Li/LNI/Mg interface in Li/LNI-Mg/LPSC/Li cells. The thickness of the LNI-Mg interlayer is 18.5 µm. The Mg element line scan in (d) is captured along the yellow line of Figure (b). (e) Galvanostatic cycling of Li/LPSC/Li cells sandwiched with LNI–25% Mg composite at constant current densities/capacity of 4mA cm^{-2} / 4mAh cm^{-2} at 25 °C.

Accomplishment 4.2: Designing a thin Li_7N_2I-Mg interlayer with gradient electronic conductivity. Reducing the thickness of the interlayer is important to increase the energy density of batteries for their practical applications. We fabricate a new type of interlayer that has gradient electronic conductivity between Li and solid electrolyte. This strategy can reduce the interlayer thickness, and increase the cell energy density and Li dendrite suppression capability.

LNI-Mg was prepared by ball-milling the LNI electrolyte and 25 wt% of Mg metal gently. The ball milling process does not change the main phase structure of LNI and Mg. As we can see from **Figure 4.2.1.a**, in XRD pattern of milled LNI-Mg, all the peaks can be assigned to LNI and Mg and no extra peak was observed. To assmeble Li/LNI-Mg/LPSC/LNI-Mg/Li batteries, 3 mg of LNI-Mg was spread on each side of LPSC electrolyte, pressed at 180 MPa and then attached Li on each side. The batteries were heated at 60 °C for 12 h. The LNI-Mg interlayer after activation was characterized. The SEM image (**Figure 4.2.1.b**) shows that the thickness of the LNI-Mg interlayer is 18.5 µm, which is much thinner than the 90 µm LNI-5%CNT interlayer. EDS mapping (**Figure 4.2.1.c**) shows that in the LNI-25%Mg interlayer Mg element diffuses to the Li anode side after activation at 60 °C for 12 hours, while I, P and S elements stay at their original position. To observe the Mg distribution in the interlayer more clearly, the line scan of the Mg element (**Figure 4.2.1.d**) was conducted along the yellow line of **Figure 4.2.1.b**. A high Mg intensity of 2500 was detected in the Li anode, suggesting the diffusion of Mg from interlayer to anode. In the interlayer, the Mg signal gradually decreases from the Li anode side to the solid electrolyte side. At the interface of the interlayer/SSE boundary, Mg intensity becomes nearly

0. Therefore, most Mg diffuses towards the Li anode side. The remaining Mg in the interlayer spontaneously forms an Mg concentration gradient (**Figure 4.2.1.d**), which generates a gradient of electronic conductivity. Briefly, by activating the Li/LPSC/Li cell with LNI-25%Mg interlayer, a gradient electronic conductive LNI-Mg interlayer was formed in situ. The Li dendrite suppression capability of the 18.5 μm gradient electronic conductive LNI-Mg interlayer was evaluated. As we can see from Figure 4.14, The Li/LPSC/Li symmetric cell with activated 18.5 μm LNI-Mg interlayer cycle at 4 mA cm^2 with a capacity of 4 mAh cm^2 for more than 100 hours at room temperature without short circuit (**Figure 4.2.1.e**). This perform is much better than CCD of 1.4 mA cm^{-2} / 1.4 mAh cm^{-2} for 14.8 μm LNI-5%CNT interlayer.

Conclusions

- The impact of lithiophobicity to Li plating and striping in the porous interlayer was simulated. It was found that increasing the lithiophobicity of the interlayer is essential to promote Li striping/plating cycling stability. Li tends to grow into or nucleate inside the interlayer if the interlayer is lithiophilic interlayer. However, Li plating and striping are self-limited in the porous lithiophobic interlayer.

- The concept of interlayer with gradient electronic conductivity was proposed to reduce interlayer thickness and improve Li dendrite suppression capability. LNI-25%Mg interlayer was prepared and formed interlayer with gradient electronic conductivity.A stable cycling of Li/LPSC/Li cell with LNI-25%Mg interlayer at a current density of 4 mA/cm^2 at a fixed capacity of 4.0 mAh/cm^2 was achieved.

- The concept of void suppression capability was proposed to evaluate the performance of Li anode. The design principle of refining grain size to boost the Li diffusivity, which is experimentally realized by the use of Mg-La inoculant into Li to form small size (~5μm) grain. The designed Li-Mg-La anode outperforms both Li and Li-Mg alloy anode, which delivered a high stripped capacity over 4 mAh/cm^2 at 0.1 mA/cm^2. The Li symmetric cell with Li-Mg-La anode showed stable cycling at 0.8 mA/cm^2.

- Different NMC size was explored to improve the coulombic efficiency and cycle life. Solid-state battery with 5 μm size NCM811 cathode can deliver 91.0 % capacity retention after 40 cycles at 0.33 C. Further utilization of NBR polymer enabled the fabrication of thin film electrolyte (<100 μm). The solid-state battery with such film electrolyte can cycle stably at 0.1 C over 50 cycles.

Key Publications

1. Hongli Wan, Zeyi Wang, Weiran Zhang, Xinzi He, Chunsheng Wang, Interface design for all-solid-state lithium batteries. *Nature*, **2023**.

2. Hongli Wan, Zeyi Wang, Sufu Liu, Tao Deng, Xinzi He, Weiran Zhang, Chunsheng Wang, Critical Interphase Overpotential as a Lithium Dendrite Suppression Criterion for All-Solid-State Lithium Battery Design. *Nat. Energy*, **2023**, 8, 473-481.

3. Zeyi Wang, J. Xia et al. Lithium Anode Interlayer Design for All-Solid-State Lithium-Metal Batteries. *Nat. Energy*. (Accepted: Nov. 2023)

4. Xiao Ji, Xinzi He, Chi Chen, Singyuk Hou, Jijian Xu, Bao Zhang, Yunjun Ruan, Jiaxun Zhang, Tao Deng, Ji Chen, Chunsheng Wang, Void Suppressive Lithium Anodes for All-Solid-State Batteries, *Nature Materials*. (Under Revision)

5. X. He, X. Ji, B. Zhang, N. Rodrigo, S. Hou, K, Gaskell, T. Deng, H. Wan, S. Liu, J. Xu, B. Nan, B, Lucht, C. Wang, Tuning interface lithiophobicity for lithium metal solid-state batteries, *ACS Energy Lett*., **2022,** 7 131-139.

6. T. Deng, X. Ji, L. Zou, O. Chiekezi, X. Fan, L. Cao, T. R. Adebisi, H. Chang, H. Wang, B. Li, X. Li, C. Wang, D. Reed, J.-G. Zhang, V. Sprenkle, C. Wang, X. Lu, Interfacial engineering enabled practical low-temperature sodium metal battery, *Nat. Nanotechnol.,* **2022,** 17, 269-277.

7. H. Wan, B. Zhang, S. Liu, J. Zhang, X. Yao, C. Wang, Understanding LiI-LiBr Catalyst Activity for Solid State Li_2S/S Reactions in an All-Solid-State Lithium Battery, *Nano Lett*. **2021**, 21, 8488-8494.

8. H. Wan, S. Liu, T. Deng, J. Xu, J. Zhang, X. He, X. Ji, X. Yao, C. Wang, Bifunctional Interphase-Enabled $Li_{10}GeP_2S_{12}$ Electrolytes for Lithium-Sulfur Battery, *ACS Energy Lett*., **2021**, 6, 862-868.

9. X. Ji, S. Hou, P-F. Wang, X. He, N. Piao, X. Fan, C. Wang, Solid-State Electrolyte Design for Lithium Dendrite Suppression, *Adv. Mater*. **2020**, 2002741.

Accomplishment 5.1: Designing high-performance anode-free solid-state batteries

In the pursuit of enhancing the energy density of all-solid-state batteries, an anode-free solid-state battery is proposed by removing the Li metal anode, since the cathode, such as $LiNi_{0.8}Co_{0.1}Mn_{0.1}O_2$ (NCM811) can act as a Li source by charging first in the initial cycle. However, the use of current collectors (CC) in solid-state batteries is an unexplored area due to the different structures and interfaces involved compared to liquid organic electrolytes. In this study, two types of current collectors, lithophobic and lithophilic, were employed to investigate Li plating and stripping behavior in Li-Cu half cells. The solid electrolyte used was Li_6PS_5Cl (LPSC), which is considered relatively more stable than other sulfide electrolytes. The current collectors were prepared using sputtering method to enable a thin (100 nm) and uniform metal layer on the copper film (~ 10 μm) surface. As Zr has no alloy phase with Cu and no reaction with sulfide electrolyte, Zr film was coated on Cu surface as the lithophilic CC. As shown in **Figure 5.1.1a-b**, at a current density of 0.5 mA cm^{-2}, the initial nucleation overpotential of Li||Cu half-cell with Zr@Cu was about 30 mV, while it decreased to 34 mV from the second cycle. This may be attributed to the establishment of the SEI layer in the first cycle. In addition, the overpotential between charge-discharge was about 37 mV, and it was slightly increased due to the increasing thickness of the SEI and side reactions between Li and LPSC. It is noteworthy the initial Coulombic efficiency (ICE) of the Li half cell with Zr@Cu was about 88%. In the first 5 cycles, the CE gradually increased due to the continuous formation of SEI, and the average CE after five cycles was 97%. As indium is widely used as the alloy metal in solid-state batteries, we used indium coated copper film as the lithophilic CC. The discharge/charge curves and CE plots of half cells with In@Cu were also exhibited in **Figure 5.1.1c-d**. The initial nucleation potential of Li||Cu half-cell with In@Cu was smaller than that with Zr@Cu, and the following nucleation potential showed no obvious change. In addition, the charge-discharge overpotential was about 27 mV. Notably, in the charging curves, there was a bending point around 0.12 V. However, although both the nucleation potential and the cycling overpotential of the half cells with In@Cu were smaller than that with Zr@Cu, the cycling behavior was not better. As shown in **Figure 5.1.1d**, the ICE of the half cells with In@Cu was only 72%, much smaller than that with Zr@Cu, which can be attributed to the alloying of thin indium film with Li in the first cycle. The alloyed Li was consumed and thereby the ICE was low. However, the CE of the following cycles was also lower, with an average value of 92.5%, indicating the continuous formation of dead Li. All these results demonstrate that the utilization of lithophobic CC Zr@Cu is more effective for realizing anode-free batteries.

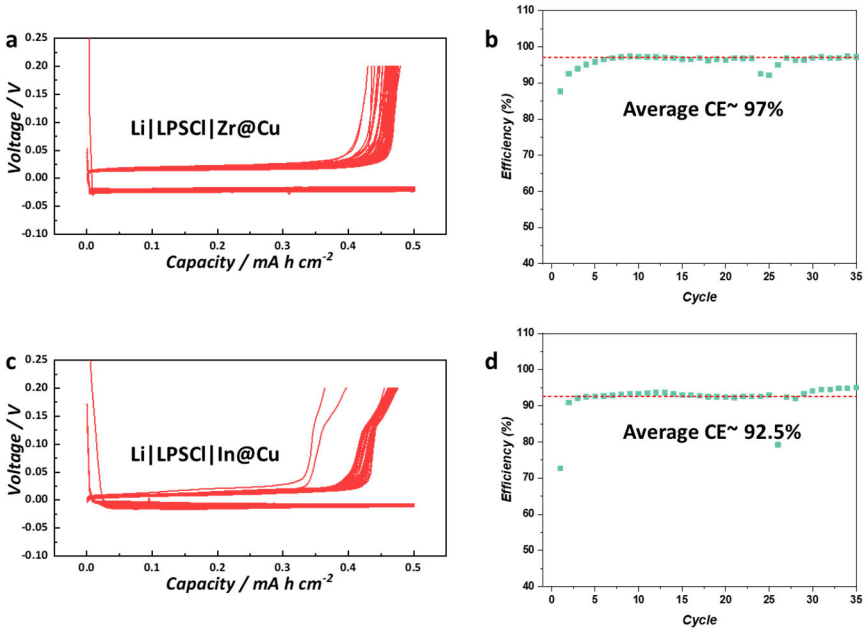

Figure 5.1.1. Discharge/charge curves and corresponding cycling Coulombic efficiency plots of Li half cells with (a, b) lithophobic current collector Zr@Cu, and (c, d) lithophilic current collector In@Cu. The current density used was 0.5 mA cm^{-2} in all tests.

The Li stress evolution in both Li-Cu half cells was further investigated through an in-situ pressure test coupled with the discharge-charge cycles of the cells (**Figure 5.1.2**). The external pressure applied to the battery was controlled within the range of 2-3 MPa. Despite the differences in the discharge-charge curves, the mechanical behavior of the cells was markedly distinct. With lithophobic Zr@Cu, the pressure changes in the single discharge/charge were about -0.35/0.42 Mpa, when the battery had a fixed 1 mAh cm^{-2} discharge capacity and was charged to 0.5 V at the current of 0.5 mA cm^{-2} (**Figure 5.1.2a**). However, there were two small bending points in the pressure-time curves, corresponding to the beginning of discharge and end of charge, which can be ascribed to the initiation of the Li nuclei and decomposition of plated Li. After Li nuclei for a capacity of 0.07 mAh cm^{-2}, the Li smoothly plated with a long straight pressure increasing curve till the end of discharge. However, at stripping, Li migrated from the intimately contacted area with a pressure-down curve, which showed a trend of decreasing slope. When Li began to disconnect, the battery voltage rapidly increased as the pressure re-increased. The pressure changes rate (dP/dt) -time plots directly revealed these trends. At the beginning of plating, dP/dt increased from -0.3 to 0.4 MPa/h, indicating the pressure first decreased and then increased. In the stable plating area, dP/dt almost kept a constant of about 0.2-0.3 MPa/h, with a slow decrease because of the growth of plated Li and hence the deformation under pressure. At stripping, dP/dt was a curve across the zero point with a single slope, which suggested that the cell had undergone the pressure drop and increase process due to the stripping of plating Li.

The pressure changes with In@Cu CC were markedly different (**Figure 5.1.2b**). The pressure of the cell with In@Cu initially dropped in the first half of plating and increased in the second half, with pressure changes of -0.16/0.10 Mpa, respectively. In the subsequent stripping, it underwent pressure changes of -0.15/0.19 MPa, corresponding to 41%/59% of the stripping process. The dP/dt revealed that the continuous change behavior across the zero point in both plating and stripping. It demonstrated that the battery did not have a stable plating or stripping behavior, probably due to the alloy reaction between In and Li, and the resulting accumulation of dead Li. Obviously, the battery with In@Cu had much more stress variation during the entire Li plating/stripping process, which was detrimental to the long-time cycling of the battery. As a result, the battery with lithophobic CC Zr@Cu is promising for the development of anode-free solid-state batteries.

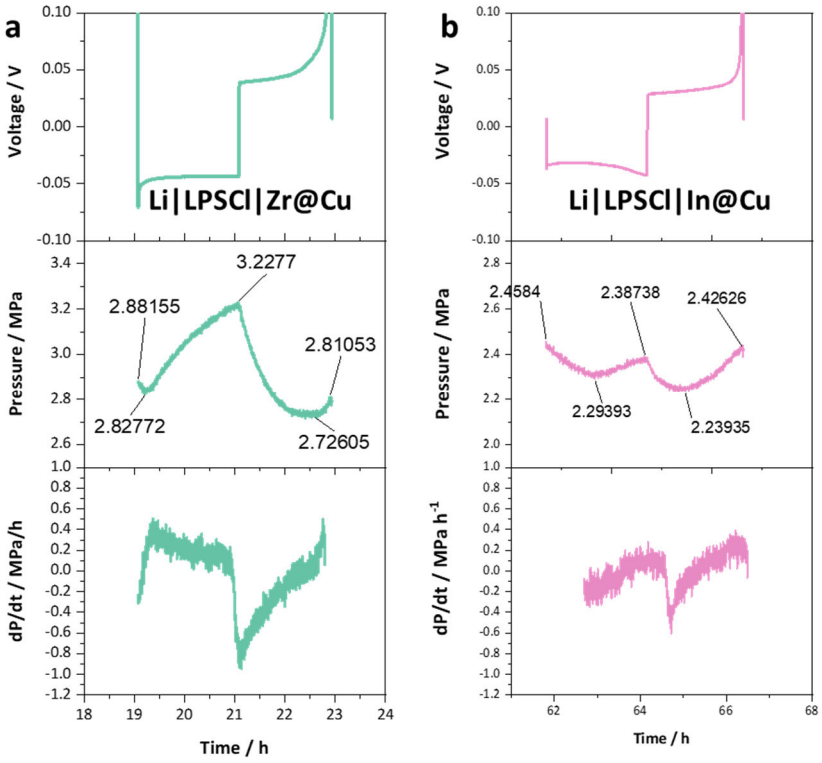

Figure 5.1.2. In-situ pressure tests of Li half cells with (a) lithophobic current collector Zr@Cu, and (b) lithophilic current collector In@Cu. The three curves in each figure are discharge/charge curves, pressure-time curves, and pressure change rate-time curves from top to bottom, respectively. The current density used was 0.5 mA cm^{-2} in all tests.

To clarify the reaction mechanism in these interfaces, we used both lithiophilic and lithiophobic current collectors as well as two different solid electrolytes (SEs) to study the electrochemical behavior of the Li-Cu half batteries. To validate the effective Columbic efficiency of Li-Cu batteries, the widely accepted testing method was adopted as shown in **Figure 5.1.3**. The Li-Cu half cells were discharged 10 hours and charged back to 0.5 V for the first cycle and discharged again 10 hours for the second cycle, after which these half cells were charged and discharge every two hours for 10 cycles and finally charged back to 0.5 V. The first cycle in this method was applied to form stable and uniform SEI layer between the deposited Li metal and SE. Then the second to last cycles were used to reversibly deposite and strip Li metal, which was recognized as a standard method to measure the Columbic efficiency of the Li-Cu half cells. In detail, as exhibited in **Figure 5.1.3 a-b**, with commercial Li_6PS_5Cl (LPSC) SE, the Li half cells with lithiophilic CC of In@Cu and lithiophobic CC of Zr@Cu showed Columbic efficiency of 94.03 % and 97.05 %, respectively. Specifically, the first cycle 10 hours discharge and charge of these two CCs had much larger difference, with a CE of 78.4 % and 91.52 % of In@Cu and Zr@Cu, respectively. It can be attributed to that LPSC SE was unstable with deposited Li and the deposited Li was sticky to the lithiophilic CC, which caused a poor first cycle CE. On the contrary, replacing lithiophilic CC with lithiophobic CC can effectively enhance the first cycle as well as the following cycling CE. As deposited Li was not adhered to lithiophobic CC, Li tended to strip back more freely. However, due to the instability of LPSC with Li, the efficiency of Li half cells with Zr@Cu was still not enough. Therefore, we further used fluorinated LPSC SE instead of LPSC to improve the CE of the half cells. As depicted in **Figure 5.1.3 c-d**, the CE of half cells with both kinds of CCs were effectively enhanced. The cycling CE of half cells with In@Cu was improved from 94.03 % to 95.93 %, when that with Zr@Cu was improved from 97.05 % to 97.70 %. In addition, the first cycle CE of half cells with In@Cu was significantly enhanced from 78.4 % to 90.25 %, while

that with Zr@Cu was also largely improved from 91.52 % to 96.17 %. Such results demonstrated that use of F-LPSC, which formed thermodynamically stable SEI of LiF, is effective and critical to enhance the CE of Li half cells. Besides, the enhancement was more effective for the initial cycle other than the following cycles, which may be attributed to the Li fatigue during cycling. However, the CE of the Li-Cu half cells with Zr@Cu and F-LPSC was still insufficient and more in-depth study of the reason for poor CE was required.

The long-term cycling of Li-Cu half cells with the aforementioned four kinds of structure were tested and shown in **Figure 5.1.4.** With LPSC SE (**Figure 5.1.4a**), the Li-half cells with Zr@Cu was stably cycled for 50 cycles with an average CE around 95.6 %. On the contrary, that with In@Cu was only stably cycled for 10 cycles with a low and decreasing CE around 90 %. After 10 cycles, this cell showed unstable cycling curves with CE vibrating in a wide range and finally decreased below 50 %. When replacing LPSC with F-LPSC, the Li-Cu half cells with both CCs had longer stable cycles. The average CE of the cells with Zr@Cu was around 97.5 % for 100 cycles while that with In@Cu was around 95 % for around 30 cycles and then decreased rapidly after 40 cycles. All these results demonstrated that the utilization of fluorinated solid electrolyte combined with lithiophobic current collector can effectively enhance the reversibility of Li deposition and dissolution during cycling. Further efforts are still required to enhance the efficiency to above 99% for the practical application of SSBs.

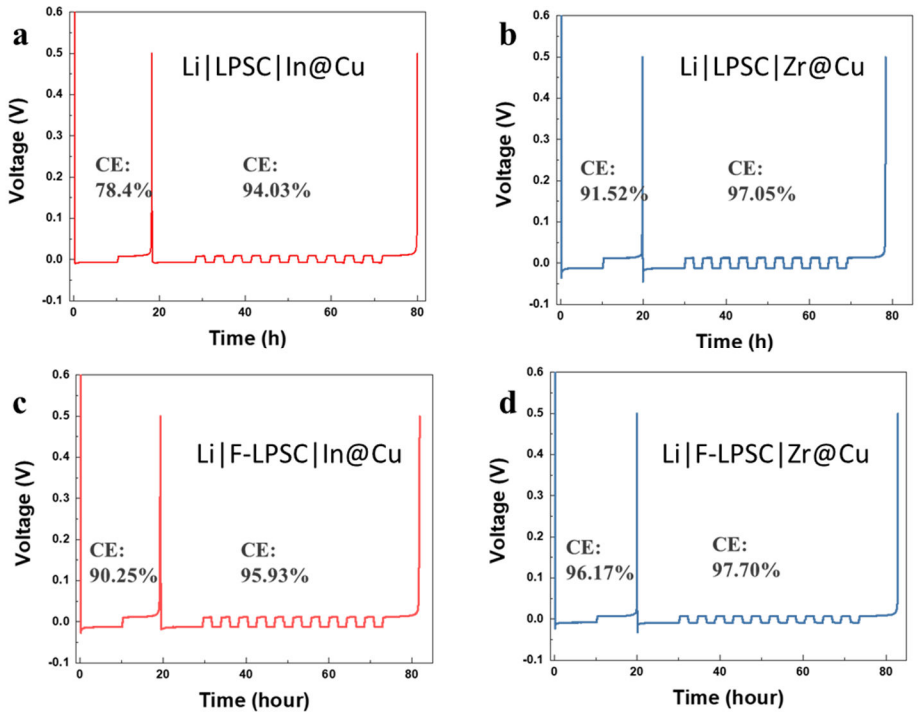

Figure 5.1.3. Discharge/charge curves of Li-Cu half cells using commercial Li_6PS_5Cl (LPSC) solid electrolyte or surface fluorinated LPSC solid electrolyte with (a, c) lithiophilic current collector In@Cu, and (b, d) lithiophobic current collector Zr@Cu. The current density used was 0.5 mA cm^{-2} in all tests.

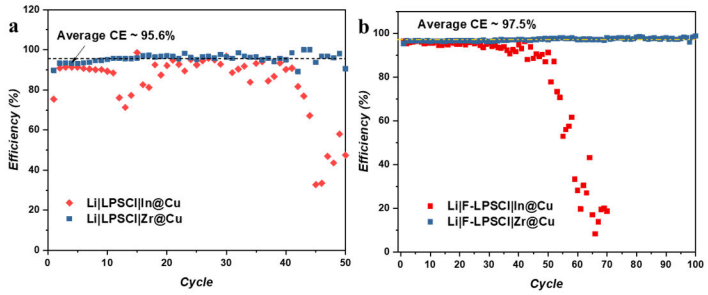

Figure 5.1.4. Cycling Coulombic efficiency plots of Li half cells with lithiophobic current collector Zr@Cu, and lithiophilic current collector In@Cu using (a) LPSC SE and (b) F-LPSC SE.

The Columbic Efficiency of Li-Cu half-cell with lithiophobic Zr@Cu was around 97.5, which is not enough for long-term stable cycling. As a result, we further studied the performance of these two kinds cells with 50% more Li in the first cycle. As depicted in **Figure 5.1.5**(a-b), the Li-Cu half-cell with lithiophobic Zr@Cu showed stable cycling over 100 hours without short circuit and first 60 hours 100 % CE, while that with lithiophilic In@Cu went to short circuit at 36 hours. This result clearly demonstrates that lithiophobic Zr@Cu still facilitate Li stripping and plating even with small amount of Li in the initial cycle. As a proof of concept, we further assembled full batteries NMC811 cathode with these two CCs. The first cycle CE of the cells with Zr@Cu and In@Cu are 69.2% and 76.5 %, respectively. After first three cycles at a small current of 0.1 C, the cells were further cycled at 0.2 C. The cell with In@Cu only maintained stable for 8 cycles and the discharge plateau suddenly dropped at 9th cycle, which indicates the dead Li remained at anode leading to the failure of Li stripping back to the cathode. On the comparison, the cell with lithiophobic Zr@Cu successfully cycled over 15 cycles with 92.8 % capacity retention. All these results demonstrate the anode-free batteries with lithiophobic current collector can potentially realize the higher energy density goal in the future.

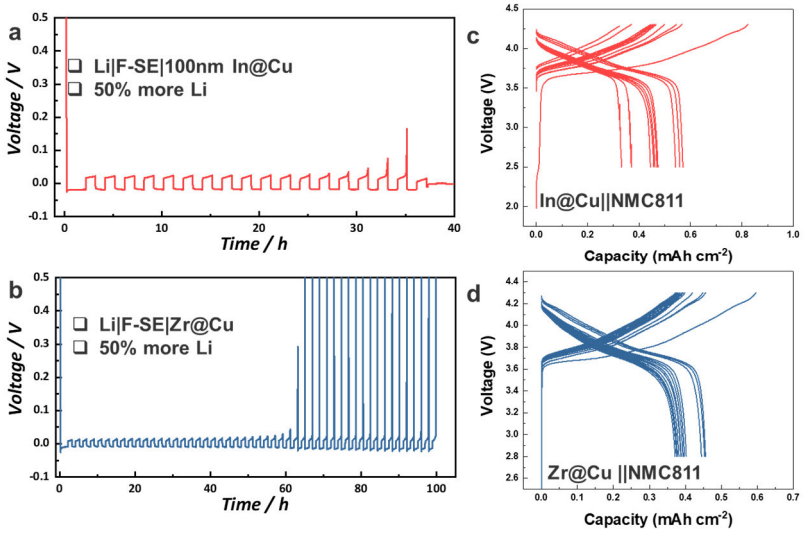

Figure 5.1.5. Li plating/stripping curves of Li-Cu half cells using surface fluorinated LPSC solid electrolyte with (a) lithiophilic current collector In@Cu, and (b) lithiophobic current collector Zr@Cu. The current density used was 0.5 mA cm^{-2}. Charge/discharge curves of NMC811 with (c) lithiophilic current collector In@Cu, and (d) lithiophobic current collector Zr@Cu. The current used in first 3 cycles were 0.1 C and in following cycles were 0.2 C.

Accomplishment 5.2: Rational design of lithium-stable halide solid electrolyte

Halide electrolyte could match with halide cathode perfectly. However, none of the halide electrolytes is thermodynamically stable against Li metal. Even worse, most halide electrolytes react with Li generating ionic insulative LiCl and electronic conductive metal in SEI, which leads to continuous side reactions and gradually increased cell overpotential. The instability issue of the halide electrolyte against Li is intricate due to a lack of comprehensive design principles. Guided by DFT calculations, we developed a halide electrolyte that is kinetically stable with lithium metal. **Figure 5.2.1a** shows the cycling performance of Li//Li cells with coated halide electrolytes. The coated Haldie solid electrolyte (cHSE) is stable against Li, achieving> 150 cycles at a current density of 0.2 mA cm^{-2} with a capacity of 0.1 mAh cm^{-2}. When the same coating layer was applied to other halide electrolytes (Li_3YCl_6, Li_3ErCl_6, $1.5Li_2O$-$HfCl_4$), the overpotential of Li//Li cell rapidly increased within ~20 cycles due to continuous side reaction. Therefore, cHSE with electronic insulative SEI is more promising to match with Li.

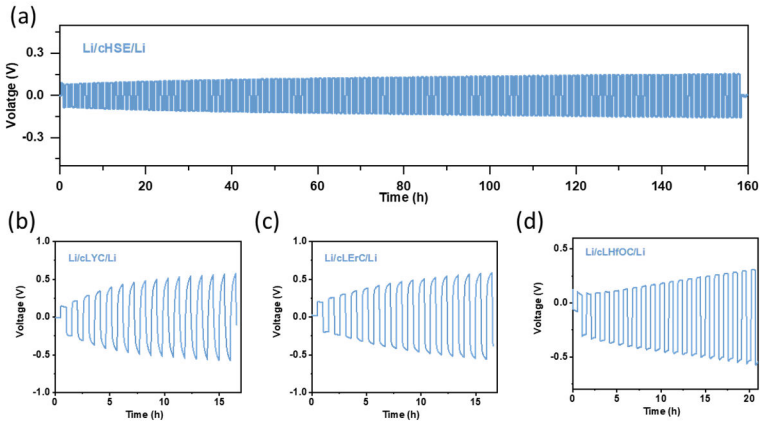

Figure 5.2.1. Cycling performance of the Li//Li cells with coated halide electrolytes: (a) designed halide electrolyte (b) Li_3YCl_6 (c) Li_3ErCl_6 (d) $1.5Li_2O$-$HfCl_4$.

Conclusions

We systematically investigated the composition of Li_xN_yI-zLiOH electrolytes (x=5, 7, 10, y=2, 3, z=0.25, 0.5, 0.75, 1) by mixing with different amount of Li_3N with LiI and LiOH. Li_5NI_2-LiOH and Li_7NI_2-LiOH were selected for further investigation. In addition, by replacing LiI with LiF, Li_3N-LiF electrolytes were also developed to investigate the Li dendrite formation mechanism. The principles of designing Li dendrite-free solid-state electrolytes have been published in *Advanced Materials* in October, 2020. The main achievements are summarized below.

- Development of Li_5NI_2-LiOH and Li_3YCl_6 solid-state electrolytes with high ionic conductivities of 0.8 and 0.5 mS/cm, respectively, reaching the milestone of > 5×10^{-4} S/cm.
- Both Li_5NI_2-LiOH and Li_7N_2I-LiOH electrolytes show a high lithium dendrite suppression capability with a critical current density of 2.0 mA/cm^2 at a capacity of 2.0 mAh/cm^2; reaching the milestone of CCD of > 2.0 mA/cm^2 at a capacity of > 2.0 mAh/cm^2.

- The Li_3N-LiF electrolyte has reached the 99% of Coulombic efficiency [*Advanced Material*s, 2020, 2002741]. The CEs of Li|Li_7N_2I-LiOH|Cu and Li|Li_5NI_2-LiOH|Cu cells are under testing.
- The electrochemical stability window is 0.0 to 2.5 V for Li_7N_2I-LiOH electrolyte and 0.0 to 5.0 V for Li_7NI_2-LiOH/Li_3YCl_6 bi-layer solid-state electrolyte.
- A Li dendrite suppression criterion has been proposed and validated in Li_3N-LiF/Li_3PS_4 based all-solid-state battery.

Key Publications

X. Ji, S. Hou, P-F. Wang, X. He, N. Piao, X. Fan, C. Wang, Solid-State Electrolyte Design for Lithium Dendrite Suppression. *Advanced Materials*, 2020, 2002741.

References

[1] X. Fan, X. Ji, F. Han, J. Yue, J. Chen, L. Chen, T. Deng, J. Jiang, C. Wang, Fluorinated solid electrolyte interphase enables highly reversible solid-state Li metal batter, *Science Advances*, **2018**, 4, eaau9245

[2] J. Yue, X. Zhu, F. Han, X. Fan, L. Wang, J. Wang, C. Wang, A Long-Cycle Life All-Solid-State Sodium Ion Battery, *ACS Applied Materials & Interfaces*, **2018**, 10, 39645

[3] R. Xu, F. Han, X. Ji, X. Fan, J. Tu, C. Wang, Interface engineering of sulfide electrolytes for all-solid-state lithium batteries, *Nano Energy*, **2018**, 53, 958

[4] X. Fan,† J. Yue,† F Han, J. Chen, T. Deng, X. Zhou, S. Hou, C. Wang, High Performance All-Solid-State Na-S Battery Enabled by Casting-Annealing Technology, *ACS Nano*, **2018**, 12, 3360

(This page intentionally left blank)

U.S. DEPARTMENT OF
ENERGY

Office of
ENERGY EFFICIENCY &
RENEWABLE ENERGY

For more information, visit:
energy.gov/vehicles

DOE/EE-#### April 2021